bioRxiv preprint doi: https://doi.org/10.1101/439331; this version posted October 9, 2018. The copyright holder for this preprint (which was not certified by peer review) is the author/funder. All rights reserved. No reuse allowed without permission.

Cell type-specific differences in protein complex stoichiometry and transcriptional regulation affect the timing of stem cell division

Natalie M. Clark[1,2,*], Adam P. Fisher[1,*], Barbara Berckmans[3], Sophia G. Zebell[4], Rüdiger Simon[3], Kimberly Gallagher[5], and Rosangela Sozzani[1,2]

1. Department of Plant and Microbial Biology, North Carolina State University, Raleigh, NC 27695 USA
2. Biomathematics Graduate Program, North Carolina State University, Raleigh, NC 27695 USA
3. Institute for Developmental Genetics, Heinrich Heine University, 40225 Düsseldorf, Germany
4. Department of Biology, Howard Hughes Medical Institute-Gordon and Betty Morre Foundation, Duke University, Durham, NC 27708 USA
5. Department of Biology, University of Pennsylvania, Philadelphia, PA, 19104 USA

*These authors contributed equally to this work

Abstract

Stem cells divide and differentiate to form all the specialized cell types and tissues in a multicellular organism. In the Arabidopsis root, stem cells are maintained in their undifferentiated state by a less mitotically dividing cell population known as the Quiescent Center (QC). However, what makes the QC fundamentally different than the actively-dividing, surrounding stem cell initials is not well understood. Here, we gained insight into differences between the QC and the Cortex Endodermis Initials (CEI) by studying the mobile transcription factor SHORTROOT (SHR) and its binding partner SCARECROW (SCR). To predict whether there are different, cell-type specific functions of SHR and SCR, we constructed an Ordinary Differential Equation (ODE) model of SHR and SCR concentrations in the QC and CEI. Using sensitivity analysis, we found that SHR and SCR complex stoichiometry as well as upstream regulation of SHR are important parameters in the model. We thus quantified SHR-SCR complex stoichiometry using scanning fluorescence correlation spectroscopy (Scanning FCS) and determined putative upstream SHR regulators using time course gene expression data. Our model prediction coupled with experimental validation showed that high levels of the SHR-SCR complex correlate with more CEI division but less QC division. Further, our model allowed us to predict the timing of QC and CEI division. Thus, our results suggest that protein complex stoichiometry and upstream transcriptional regulation modulate the division timing of different specialized cell types.

bioRxiv preprint doi: https://doi.org/10.1101/439331; this version posted October 9, 2018. The copyright holder for this preprint (which was not certified by peer review) is the author/funder. All rights reserved. No reuse allowed without permission.

Introduction

The tight, coordinated regulation of stem cell division and differentiation ensures proper development and growth of multicellular organisms. In the Arabidopsis root stem cell niche (SCN), tightly controlled asymmetric divisions regenerate the stem cells and produce all of the differentiated tissues from different stem cell populations. The Arabidopsis root SCN also contains a relatively mitotically inactive cell population, known as the Quiescent Center (QC), which is thought to maintain the surrounding initials in an undifferentiated state (1, 2). Thus, determining how the QC regulates the surrounding stem cells, or what makes the QC fundamentally different from the actively dividing initials, is important for understanding how stem cell division is controlled and maintained during development.

Mobile signals including transcription factors (TFs) have been shown to have regulatory roles in the Arabidopsis root SCN (3–5). Specifically, the mobile TF SHORTROOT (SHR) has a key role in controlling Cortex Endodermis Initial (CEI) division. After SHR is transcribed in the vasculature, its protein moves to the CEI cells where it forms a complex with another transcription factor, SCARECROW (SCR). SHR and SCR control CEI division through the regulation of CYCLIND6;1 (CYCD6;1) (3, 6–12). In addition to their role in the CEI, SHR and SCR have known roles in the endodermis, where along members of the C2H2 zinc finger family of TFs (the BIRD proteins), regulate ground tissue specification and division (9, 13–16).

It has been shown that SHR movement is restricted in order to confine cell division to certain tissues and cells in the root. For example, in a SCR RNAi (SCRi) line, SHR can move past the endodermis and into the cortex layer, causing extra divisions (17, 18). Quantitative work using Scanning Fluorescence Correlation Spectroscopy (Scanning FCS) expanded on this observation to show that SHR protein additionally moves back to the vasculature in the absence of SCR (19) Therefore, it was suggested that the SHR-SCR complex acts to spatially restrict SHR expression, and thus cell division, to the endodermis. In addition, recent work has shown that two members of the BIRD family named JACKDAW (JKD) and BALDIBIS also bind to SCR to restrict SHR movement past the endodermal cell layer of the ground tissue and confer endodermal fate (14). Therefore, the regulation of SHR movement through its binding with SCR and the BIRDs is an important mechanism for restricting cell division in the Arabidopsis root.

SHR also moves into, and binds SCR, in the QC. While recent work used FRET-FLIM to show that both the SHR-SCR and SHR-JKD complexes form in the QC, with the SHR-JKD complex contributing to QC specification and maintenance (9), it is still unclear how the SHR-SCR complex may contribute to QC division as the QC is relatively mitotically inactive. One hypothesis is that the oligomeric state of SHR and SCR and stoichiometry of the SHR-SCR protein complex could affect its function, as this is the case with other protein complexes in Arabidopsis (20, 21). It has already been shown that the SHR-SCR stoichiometry may be important for its function in the endodermis, as the SHR-SCR complex exists in both a 1 SHR: 1

bioRxiv preprint doi: https://doi.org/10.1101/439331; this version posted October 9, 2018. The copyright holder for this preprint (which was not certified by peer review) is the author/funder. All rights reserved. No reuse allowed without permission.

SCR and 2 SHR: 1 SCR stoichiometry. Also, it has been shown that SHR homodimer formation in the endodermis depends on the presence of SCR (19). Therefore, determining the oligomeric state and protein complex stoichiometry of SHR and SCR proteins would increase our understanding of their differing roles in QC and CEI division.

Here, we show how differences in transcriptional regulation and protein complex stoichiometry of SHR and SCR affect their roles in QC and CEI division. We first used scanning FCS to show that SHR and SCR form complexes with 4 different stoichiometries in the QC, as compared to 2 in the CEI. We then incorporated these experimental results into an Ordinary Differential Equation (ODE) model of SHR and SCR expression in the QC and CEI. This model included production parameters, such as the production of a putative SHR activator and repressor, which were estimated from meristematic time course gene expression data. We then used our model to predict if the SHR-SCR complex functions differently between the QC and CEI. Using a combination of modeling and experimental validation, we showed how the SHR-SCR complex could promote CEI division but represses QC division. Further, our model allowed us to determine the relative timing of CEI and QC division in the root. Overall, our model provides a framework for how the upstream regulators of SHR, the SHR-SCR complex, and the cell-specific complex stoichiometries regulate the timing of QC and CEI division.

Results

Protein oligomeric state and complex stoichiometry are important parameters in a model of SHR and SCR expression dynamics

To address if the temporal dynamics, and potentially the biological role, of the SHR-SCR complex is different between the QC and CEI, we developed an ordinary differential equation (ODE) model that predicts SHR and SCR levels in the QC and CEI. For simplicity, we modeled transcriptional regulation and protein expression in the same equation. Our model includes SHR movement from the stele into the QC and CEI (3, 19). This model also assumes that SHR and SCR can oligomerize with themselves to form homodimers, as well as heterodimerize with each other to form protein complexes with various stoichiometries (e.g. 1 SHR: 1 SCR, 2 SHR: 1 SCR, etc.) (19). In addition, we incorporated the known upstream activation of SCR by the SHR:SCR complex (17). Finally, as also suggested by (22), we considered that SHR and SCR could be regulated by unknown, upstream factors and incorporated a SCR repressor, SHR activator, and SHR repressor (see Methods, Supplementary Information).

To develop the most accurate model, we first performed a global sensitivity analysis to identify the most important parameters in the model and, thus, the parameters that needed to be experimentally determined or estimated from data (see Methods, Supplementary Figure 1, Supplementary Table 1). We found that 14 out of the 26 parameters were sensitive, which include: the SHR diffusion coefficient, SHR and SCR homodimer and heterodimer formation, SHR and SCR production terms, and upstream SHR regulation. We set the remaining 12

bioRxiv preprint doi: https://doi.org/10.1101/439331; this version posted October 9, 2018. The copyright holder for this preprint (which was not certified by peer review) is the author/funder. All rights reserved. No reuse allowed without permission.

parameters to constant values, as variations in these parameter values do not significantly impact the model outcome.

We first focused on determining the SHR diffusion coefficient, oligomeric state, and complex stoichiometries using scanning Fluorescence Correlation Spectroscopy (Scanning FCS). We previously calculated that SHR moves into the endodermis and CEI at a rate of 2.45 μm^2/sec and into the QC at a rate of 1.73 μm^2/sec using Raster Image Correlation Spectroscopy (RICS) (19). Next, to experimentally determine the oligomeric state of SHR and SCR in the QC and CEI, we quantified the percentage of monomeric and homodimeric forms of either SHR:SHR-GFP or SCR:SCR-GFP translational fusions using Number and Brightness (N&B; see Methods). These SHR and SCR monomers and homodimers may be free, or they may bind each other to form heterodimeric or higher complexes. We found that there is significantly more SHR and SCR homodimer in the QC (16.9% SHR homodimer, 17.3% SCR homodimer) than in the CEI (11.3% SHR homodimer, 6.6% SCR homodimer) (Figure 1A). Next, to determine if the SHR-SCR complex stoichiometry varies between the QC and CEI we performed cross-correlation number & brightness (cross N&B; see Methods) on roots expressing both the SHR:SHR-GFP and SCR:SCR-mCherry translational fusions (Figure 1D). The output of cross N&B is a stoichiometry histogram that gives qualitative information about the amount of SHR-SCR binding. To quantitatively assess the different protein complexes, we developed a binding score using this histogram in which a high score (6, red line) corresponded to a high association between SHR and SCR and a low score (1 or 0, dark blue line or no line) corresponded to no association between SHR and SCR (Supplemental Figure 2, see Methods). We found that the number of different stoichiometries, as well as their abundance, varies between the QC and the CEI. Notably, the complexes incorporating SCR homodimer (namely 1 SHR: 2 SCR and 2 SHR: 2 SCR) have higher binding scores in the QC than the CEI, suggesting that these complexes are more likely to form in the QC. In support of this, we find that the second most abundant complex in the QC is 1 SHR: 2 SCR, while the second most abundant complex in the CEI is 2 SHR: 1 SCR. In addition, the 2 SHR: 2 SCR complex does not form in the CEI (Figure 1B). Thus, both the percentage of oligomeric states and stoichiometries of the SHR-SCR complex are significantly different between the QC and CEI, suggesting different roles for SHR and SCR in these two cells.

With this experimental data, we returned to our model and estimated the formation parameters for the SHR and SCR homo- and heterodimers such that our model recapitulates the experimentally measured proportions of these complexes (Supplemental Table 2). Given the complete absence of the 2 SHR: 2 SCR complex and the low (<5%) amount of 1 SHR: 2 SCR complex in the CEI, we simplified the model and assumed that these complexes do not form in the CEI. In addition, we incorporated our previously measured diffusion coefficient of SHR into the QC and CEI (19). Finally, we collected a stem cell-enriched population from the root meristem every 8 hours from 4 days to 6 days after plating (hereinafter referred to as the stem

bioRxiv preprint doi: https://doi.org/10.1101/439331; this version posted October 9, 2018. The copyright holder for this preprint (which was not certified by peer review) is the author/funder. All rights reserved. No reuse allowed without permission.

cell time course) to determine the temporal expression of SHR and SCR (Supplemental Table 3, Supplemental Figure 1, see Methods). We then used these data to estimate values for the production terms of SHR and SCR monomers in our model.

Model incorporates production parameters of a putative SHR activator and repressor

In order to estimate the production parameters of the upstream SHR and SCR regulators, we first needed to determine the best values of those parameters that would most accurately recapitulate our SHR and SCR time course data. To this end, we set the production parameters of the upstream SHR and SCR regulators to minimize the error between the model and our data (Supplemental Table 2, Supplemental Figure 3). This best-fitting model not only predicted the expression of SHR and SCR but also of their upstream regulators (Supplementary Figure 3). Thus, we reasoned that we could use our model prediction to identify the putative upstream transcriptional regulators of SHR and SCR and re-estimate these parameters using biological data.

We first identified putative candidates for the SHR activator by generating a list of 21 transcription factors (TFs) that were either shown to directly bind the SHR promoter (through Chromatin Immunoprecipitation (ChIP) or Yeast-1-Hybrid (Y1H)), or whose mutant/overexpression lines show a decrease/increase in SHR expression (22–25) (Supplementary Figure 4, Supplementary Table 4). We then compared the time course data of these TFs from our stem cell time course to the model prediction for the SHR activator. To quantify the goodness of fit between the experimental expression and model prediction, we calculated a sign score for each TF, which measures whether the experimental data and the model prediction vary in the same direction. A sign score of 1 corresponded to when the model and expression of the TF changed in the same direction (either increasing or decreasing); whereas a sign score of -1 corresponded to a gene whose expression changed in the opposite direction predicted by the model (see Methods). As a result, we identified 6 genes, STOREKEEPER 1 (STK01), HOMEOBOX 13 (HB13), SEUSS (SEU), bZIP17, ETHYLENE RESPONSIVE ELEMENT BINDING FACTOR 4 (ERF4), and AT3G60580, which all had the highest possible sign score (sign score = 5) and represented candidates for activation of SHR (Supplementary Figure 4, Supplementary Table 4).

To test these 6 putative SHR activators, we first determined if SHR expression changes in their mutant lines. Previous work showed that *bzip17* and *stk01* have an approximately 2-fold decrease in levels of SHR as measured by qPCR (22). We also found that SHR was one of the 3263 genes whose expression was significantly lower (3-fold) in the *seu-3* mutant (Figure 2B, Supplementary Table 5). We next examined if these 3 mutants show a stem cell niche phenotype, as this would suggest these TFs specifically regulate SHR in the stem cells. While neither *stk01* nor the *bzip17* mutants showed phenotypes, we found that *seu-3* mutants showed a disorganized root stem cell niche, including improperly maintained columella stem cells (as shown by starch

bioRxiv preprint doi: https://doi.org/10.1101/439331; this version posted October 9, 2018. The copyright holder for this preprint (which was not certified by peer review) is the author/funder. All rights reserved. No reuse allowed without permission.

granules accumulation in columella layer just below the QC) (Figure 2B, Supplementary Figure 5,6). Therefore, the transcriptional and phenotypic data support our model prediction that SEU putatively activates SHR.

Although it was shown that SEU directly binds the SHR promoter (25), SEU is a known transcriptional adapter (26) and therefore likely requires a binding partner to transcriptionally regulate SHR. To identify potential SEU interactors, we completed a Yeast Two-Hybrid (Y2H) screen using SEU as the bait against a TF library generated in (22) (Supplementary Table 6). Since the binding partner should have expression that matches the SHR activator, we looked at the expression of each of the 21 candidate interactors from our stem cell time course and compared it to the model prediction. We found that only 2 TFs, SCR and TMO5-LIKE1 (T5L1), had the maximum possible sign score (sign score = 5), suggesting that these 2 genes represent the most likely binding partners of SEU (Supplementary Figure 7, Supplementary Table 7). Using Cross N&B, we were able to validate that the SEU-SCR complex forms in the QC and CEI (Supplementary Figure 8). Given that SEU is expressed throughout the root (Supplementary Figure 8), we reasoned that the binding partner of SEU should be expressed specifically in the stele to regulate SHR in a tissue-type specific manner. Accordingly, we identified T5L1 as enriched in the xylem cell-type specific data (27) (Supplementary Figure 7), suggesting that T5L1 is a vasculature-specific binding partner of SEU. Further, using qPCR we found that SHR is 7-fold lower in the *t5l1* mutant (Supplementary Figure 7), supporting that T5L1 activates SHR. Finally, we observed overall stem cell niche disorganization in the *t5l1* mutant (Supplementary Figure 7), consistent with the hypothesis that T5L1 binds to SEU to regulate SHR expression.

We next focused on identifying putative SHR repressors using the sign score measurement and obtained a list of 25 candidates from similar sources as the SHR activators (Supplementary Table 4). Out of these 25 putative repressors, only NAC13 had the highest possible sign score of 5 (Supplementary Figure 9). However, NAC13 expression is enriched in the mature xylem cells compared to the meristematic vasculature cells (Supplementary Figure 9) (28). This suggests that NAC13 may repress SHR higher up in the root, but it is not involved in the meristematic regulation of SHR. Thus, to identify additional putative SHR repressors in the meristematic region, we searched for genes expressed in the stele initials as well as other stem cells, as proteins could move to the stele initials to regulate SHR. We performed Fluorescence Activated Cell Sorting (FACS) using a marker line that is expressed in all of the stem cell populations (AGL42:GFP (29)) and collected the GFP positive cells as well as the GFP negative cells, which in this case constitute the pool of non-stem cells (Supplementary Figure 10, see Methods). We performed RNA-seq and identified 125 TFs significantly enriched in the stem cells compared to the non-stem cells and calculated their sign score when compared to the model prediction of the SHR repressor (Supplementary Table 8, see Methods). WUSCHEL-RELATED HOMEOBOX 5 (WOX5) was the only TF that had the highest possible sign score of 5 (Figure 2F, Supplementary Table 8), suggesting that WOX5 is a putative repressor of SHR.

bioRxiv preprint doi: https://doi.org/10.1101/439331; this version posted October 9, 2018. The copyright holder for this preprint (which was not certified by peer review) is the author/funder. All rights reserved. No reuse allowed without permission.

WOX5 expression is barely detected in the vasculature (27, 30, 31), so we asked if WOX5 protein localization in the vascular initials could be due to WOX5 movement from the QC (Figure 2C). To this end, we performed Pair Correlation Function (pCF) analysis on the WOX5:WOX5-GFP translational fusion and compared its movement to a protein that is able to move (35S:GFP) and a protein that is not able to move (TMO5:3xGFP) from the QC to the vascular initials (19) (see Methods). We found that the WOX5 protein moves from the QC to the vascular initials with a movement index (MI) of 0.75 ± 0.06, which is significantly higher than the movement index of our non-mobile control protein (TMO5:3xGFP, MI= 0.27 ± 0.07) (Figure 2C). These data are consistent with WOX5 movement from the QC to the vascular initials. To test if WOX5 is a putative regulator of SHR, we performed RNA-seq on a *wox5-1* mutant line and found that SHR is one of the 3302 genes that had higher expression when compared to wild type, suggesting that WOX5 represses SHR (Figure 2B, Supplementary Table 9). These results, together with the well-documented root phenotype in the *wox5-1* mutant (Figure 2B, Sarkar et al., 2007), support that WOX5 represses SHR in the vascular initials.

Model shows how SHR-SCR complex levels modulate the timing of CEI division

After estimating the production parameters of the SHR activator and repressor using SEU and WOX5 expression data from the stem cell time course, respectively (Supplementary Table 10), we used the model to predict the function of SHR and SCR in the QC and CEI (Supplementary Figure 11). We specifically used the model to see how the proportions of the complex stoichiometries change over time, as this is information that is not provided by our stem cell time course and cross N&B data. First, in the CEI our model predicts that both the 1 SHR: 1 SCR and 2 SHR: 1 SCR stoichiometries reach their maximum value between 4 days 8 hours (4D 8H) and 4 days 16 hours (4D 16H) after plating. After 4D a decrease in the expression of SHR and SCR correlates with a decrease in the levels of both the 1 SHR: 1 SCR and 2 SHR: 1 SCR stoichiometries (Figure 3A, Supplementary Figure 10). Based on previous results showing that high levels of the SHR-SCR complex trigger CEI division, and that CEI division occurs roughly around 5 days (5D) (7), we hypothesized that high levels of the SHR-SCR complex induce CEI division between 4D 16H and 5D. To test this hypothesis, we observed the expression of the CYCD6 marker (pCYCD6::GUS-GFP), which is expressed immediately preceding CEI division (7), in 5D old roots and found that 77.8% of roots show pCYCD6::GUS-GFP expression, suggesting that most of the CEI are undergoing periclinal division at 5D (Figure 3B). After this CEI division at 5D, our model predicts that both stoichiometries (1 SHR: 1 SCR and 2 SHR: 2 SCR) of the SHR-SCR complex reach their highest levels by 5 days 8 hours (5D 8H) but then quickly decline. Between 5 days 16 hours (5D 16H) and 6 days (6D), the total SHR-SCR complex level in the CEI is predicted to be 1.5- to 2-fold lower than between 4D 16H and 5D, which is when we know that the CEI divides (Figure 3A). Therefore, we hypothesized that the relatively low levels of the SHR-SCR complex could correlate to less CEI division. To test this, we observed pCYCD6:GUS-GFP at 6D and found that only 18.2% of roots expressed the

bioRxiv preprint doi: https://doi.org/10.1101/439331; this version posted October 9, 2018. The copyright holder for this preprint (which was not certified by peer review) is the author/funder. All rights reserved. No reuse allowed without permission.

CYCD6 marker compared to 77.78% of the roots at 5D (Figure 3B). Altogether, our model and experimental data suggest that high levels of both SHR-SCR stoichiometries correlate with more CEI division at 5D, but that all CEI have periclinally divided by 6D, which halts the normal asymmetric division of the CEI.

We next used our model to predict how changes in the upstream regulators of SHR could affect SHR dynamics and consequently CEI division. We first observed how SHR expression changed in the model when we individually removed SEU or WOX5 production. The model predicted that roots with no SEU production should have lower SHR expression, while roots with no WOX5 production should have more SHR expression (Figure 3C). This agreed with our biological data, which show lower SHR expression in *seu-3* mutants and higher SHR expression in *wox5-1* mutants (Figure 2B). We next used the model to infer what happened to SHR expression when both SEU and WOX5 were removed. Our model suggested that SHR expression is increased when there is no production of both SEU and WOX5 to the same extent as when there is no production of only WOX5, such that SHR expression in *seu-3 wox5-1* double mutants should be the same as in *wox5-1* single mutants. (Figure 3C). To test the accuracy of the model prediction, we performed qPCR on the *seu-3 wox5-1* double mutant and compared the change in SHR to our RNA-seq data of the *wox5-1* single mutant. We found that *seu-3 wox5-1* mutants have approximately 2-fold higher SHR expression (Figure 3C), which was a similar increase in SHR compared to the *wox5-1* single mutant (1.7-fold, Figure 2B). To further determine how changes in SEU and WOX5 expression affect cell division, we again used the CYCD6 marker as a proxy for SHR expression and CEI division and quantified the number of roots that show low, medium, or high CYCD6 expression (see Methods). At 5D, we found that *wox5-1* mutants had more roots with high CYCD6 expression compared to wild type plants (63.16% of *wox5-1* mutant roots compared to 13.33% of wild type roots) (Figure 3D), which supported our model prediction that less WOX5 correlates with higher SHR expression. While *seu-3 wox5-1* double mutants also had a higher percentage of roots with high CYCD6 expression compared to wild type (41.18% of *seu-3 wox5-1* roots), this proportion of roots with high expression was not statistically different from the *wox5-1* single mutant roots (Figure 3D), which supported the additional model prediction that the double mutant has the same effect as the single *wox5-1* mutant. Overall, these results suggest that the repressive activity of WOX5 has a greater effect on SHR expression in the CEI than the activation of SEU.

SHR and SCR form more complex stoichiometries in the QC and repress QC division

Given that QC cells are less mitotically active and divide at a lower rate than the CEI (32), we used our model to predict if changes in SHR-SCR complex stoichiometries could correlate with fewer QC divisions. Unlike in the CEI, our cross N&B analysis showed that the SHR-SCR complex forms 4 stoichiometries in the QC, namely 1 SHR: 1 SCR, 2 SHR: 1 SCR, 1 SHR: 2 SCR, and 2 SHR: 2 SCR (Figure 4A). Our model predicts that levels of all of the SHR-SCR complex stoichiometries in the QC reach their highest value around 4D 16H and decrease

bioRxiv preprint doi: https://doi.org/10.1101/439331; this version posted October 9, 2018. The copyright holder for this preprint (which was not certified by peer review) is the author/funder. All rights reserved. No reuse allowed without permission.

afterward (Figure 4A). We examined twenty-five 5D roots and found that none (0%) have QC divisions, suggesting that the high SHR-SCR levels in the QC do not correlate with QC division. We thus incorporated these results into our model by assuming that the QC does not divide at 5D (see Methods). We observed that all of the different SHR-SCR stoichiometries reach their highest value around 5D 8H in the QC and quickly decrease afterwards (Figure 4A). Since the model shows that levels of the SHR and SCR transcript, and by extension all the SHR-SCR complex stoichiometries, reach their lowest values at 6D (Figure 4A), we reasoned that this minimum value of the SHR-SCR complex levels in the QC at 6D may promote QC divisions. To test this hypothesis, we measured the expression of SHR:SHR-GFP and SCR:SCR-GFP translational reporters in brassinolide (BL)-treated plants, as it has been shown that BL-treated roots have increased QC divisions (33). We found that the levels of SHR and SCR proteins are significantly reduced in BL-treated plants at 5D (Figure 4B), and this reduction of SHR and SCR in BL-treated plants corresponds to more QC divisions, as 26.9% of 5D and 67.9% of 6D BL-treated roots showed QC divisions (Supplemental Figure 12). In addition, we examined a SCR RNAi line (SCRi) line where SCR levels are 60% lower than in WT plants (17) and found that 45% of roots have QC divisions 5 days after plating, further supporting that lower levels of SCR correlate with QC division (Supplementary Figure 12). Finally, we examined the WOX5:WOX5-GFP translational fusion in 5D-old BL-treated roots and found not only that WOX5 accumulation is 2-fold higher in BL treated plants compared to control plants but also that the domain of accumulation of WOX5 is expanded higher in the stele (Figure 4C). These results further support our model prediction that WOX5 represses SHR in the stele. Thus, while the SHR-SCR complex promotes periclinal division in the CEI, our results suggest that this complex represses division in the QC.

We next used the model to determine how the proportions of the different SHR-SCR stoichiometries affect CEI and QC division. Our model predicts that the 1 SHR: 1 SCR and 2 SHR: 1 SCR stoichiometries are always expressed (expression > 0) in the CEI, even at 6D when the CEI does not divide (Figure 3A). This suggests that the levels of both the 1 SHR:1 SCR and 2 SHR:1 SCR complexes are important for regulating CEI division. In the QC, our model predicts that the two complexes incorporating SHR homodimer, namely 2 SHR:1 SCR and 2 SHR: 2 SCR, are not present (expression = 0) at 6D (Figure 4A). Thus, we performed Cross Number and Brightness (Cross N&B) on SHR and SCR in BL-treated roots to determine whether the relative levels of the different SHR-SCR complexes change in the more mitotically active QC. As the model predicted, we found both the 2 SHR:1 SCR and 2 SHR: 2 SCR complex no longer form in the QC of BL treated plants (Figure 4D). Further, we examined SHR:SHR-GFP plants and found that only a small amount of SHR dimer (< 2%) forms in BL-treated plants, suggesting that the loss of these stoichiometries in BL-treated plants is due to the loss of SHR dimer (Supplemental Figure 13). Therefore, our results suggest that repression of QC division may depend on the SHR-SCR complex stoichiometries that incorporate the SHR homodimer, namely the 2 SHR: 1 SCR and 2 SHR: 2 SCR complexes.

bioRxiv preprint doi: https://doi.org/10.1101/439331; this version posted October 9, 2018. The copyright holder for this preprint (which was not certified by peer review) is the author/funder. All rights reserved. No reuse allowed without permission.

Discussion

SHORTROOT (SHR) and SCARECROW (SCR) are known regulators of Cortex Endodermal Initial (CEI) division, but their role in the less mitotically dividing cells, such as the Quiescent Center (QC), is less well understood. By combining mathematical modeling and experimental data, we showed how both levels of SHR and SCR transcripts and differences in the stoichiometry of the SHR-SCR complex correlated with differences in CEI and QC division. Together, our model and data supported that high levels of the SHR and SCR complex promote CEI but repress QC divisions (Figure 5).

Sensitivity analysis on our mathematical model identified several parameters that were important for predicting SHR and SCR expression dynamics in the CEI and QC, specifically the production and degradation rates of the different oligomeric states and protein complex stoichiometries. Other examples of proteins that form higher oligomers are Arabidopsis ethylene receptors, which use disulfide bonds to form higher oligomeric states. Disrupting these disulfide bonds greatly affects the receptors' ability to bind ethylene (21). In another case, the receptors CLAVATA 1 (CLV1) and ARABIDOPSIS CRINKLY 4 (ACR4) form homo- and heterodimeric complexes which differ in their predicted stoichiometries depending on their localization at the plasma membrane or plasmodesmata (34). We have previously shown that the formation of SHR homodimers in the endodermis depends on the presence of SCR (19). Future work could investigate if the binding of SCR to SHR causes a conformational change in SHR that allows it to form a homodimer, contributing to cell-type specific functions.

In addition to using our model to determine how SHR and SCR regulate CEI and QC division, we were also able to predict the timing of these divisions. Our model predicts that the CEI division occurs at 5D after plating, which is supported by additional data showing that SHR and SCR levels are induced in the CEI in 5D-old roots (7). Our data also show that CEI division occurs at 4D (Figure 3B), supporting that these divisions normally happen at least once every 24 hours. However, significantly less roots undergoing CEI division at 6 days corresponds to a low level of SHR-SCR complex and CYCD6 expression (Figure 3B, Figure 5), suggesting that all of the CEI are periclinally divided at this time. We were also able to use our model to show that low levels of SHR and SCR correlate with QC division (Figure 4). While previous work has shown that SCR has a role in QC identity (35), this is a new insight on how these two genes may regulate QC division. In addition, previous work has shown that the QC cells divide at roughly half the rate of the CEI (32). Therefore, given its slower division rate, we can only speculate that the QC takes longer to divide, perhaps dividing at up to 7 days after plating (Figure 5). While we have a clear marker of CEI division (CYCD6), we currently do not have a similar marker for the QC. Moreover, previous work has shown that brassinolide (BL) treated plants have excessive QC divisions that correlate with a lower level of the cell cycle inhibitor ICK2 (36). Given our results showing that BL-treated plants also have lower SHR and SCR levels (Figure 4B), it would be important but beyond the scope of this work to investigate whether SHR and SCR

bioRxiv preprint doi: https://doi.org/10.1101/439331; this version posted October 9, 2018. The copyright holder for this preprint (which was not certified by peer review) is the author/funder. All rights reserved. No reuse allowed without permission.

regulate ICK2 to inhibit division of the QC. Additional work could be done to study the role of CYCLIN D 3;3 (CYCD3;3), which is normally expressed outside of the QC but is expressed in the QC in a *wox5-1* mutant (37). We propose that WOX5 represses SHR and SCR in the vascular initials, so it is possible that the increase in CYCD3;3 in *wox5-1* mutants could be due to an increase in SHR and SCR levels. Finally, mutants in CELL CYCLE SWITCH 52 A2 (CCS52A2) have excessive QC divisions and a disorganized stem cell niche(38, 39), so SHR and SCR could additionally activate CCS52A2 to prevent QC division. Thus, future work could identify whether SHR and SCR regulate ICK2, CYCD3;3, CCS52A2, or other cell cycle genes in the QC to control its division.

We were able to leverage our model to identify two putative SHR regulators, namely SEUSS (SEU) and WUSCHEL-RELATED HOMEOBOX 5 (WOX5). SEU, with its binding partner TMO5-LIKE 1 (T5L1), transcriptionally activates SHR in the vasculature. Additionally, WOX5 protein moves from the QC into the vascular initials to repress SHR (Figure 5). We believe that our model prediction can be further used to identify additional upstream SHR and SCR regulators, which are not limited to those three genes. For the SHR activator, we used a set of transcription factors that have been shown to affect SHR expression. As more transcription factors are identified as potential SHR regulators, we can use our model prediction and sign score analysis to test if these putative SHR regulators should be kept in consideration. In addition, SHR is expressed in a gradient, with its highest expression at the tip of the root (11). Thus, potential regulators of SHR may be expressed in the same gradient as SHR, and datasets measuring gene expression gradients in the root could be used to identify additional putative SHR regulators (40). Similar techniques could be used to identify upstream SCR regulators, increasing our understanding of how this regulatory network controls CEI and QC divisions.

Here, we used a quantitative approach of iterating mathematical modeling with heterogenous experimental methods to show the differing roles of SHR and SCR in the QC and CEI. Specifically, we integrated imaging and gene expression data to quantify SHR-SCR complex stoichiometry, identify putative upstream regulators of SHR, and predict the timing of QC and CEI divisions (Figure 5). While we anticipate that other factors are needed to regulate stem cell division in the Arabidopsis root, our work provides new insights into how SHR and SCR are involved in this process. In conclusion, our results highlight how protein-protein complex stoichiometry and transcriptional regulation contribute to differential TF regulation of division between specialized cell types.

Methods

Plant lines used in this study

The *wox5-1, seu-3, stk01, bzip17, t5l1,* and SCRi lines are previously described in (17, 22, 30, 41, 42). The 35S:GFP; UBQ10:mCherry; SHR:SHR-GFP; SCR:SCR-GFP; SHR:SHR-GFP,

bioRxiv preprint doi: https://doi.org/10.1101/439331; this version posted October 9, 2018. The copyright holder for this preprint (which was not certified by peer review) is the author/funder. All rights reserved. No reuse allowed without permission.

SCR:SCR:mCherry; and TMO5:3xGFP lines are described in (19). The WOX5:WOX5-GFP line is described in (4), the pCYCD6:GUS-GFP line is described in (7), and the SEU:SEU-GFP line is described in (43).

Standard molecular biology protocols and Gateway (Invitrogen) technology were followed to obtain expression clones. Open reading frame of the WOX5 promoter (4653 bp upstream of the ATG) and gene was amplified from a genomic DNA template with Pfu DNA Polymerase (Promega). All primers used for ORF and promoter isolation are listed in Supplementary Table 13. pENTR™5′-TOPO and pENTR/D-TOPO were used to generate WOX5 promoter and gDNA entry clones, respectively. The entry clone for GFP was obtained from the PSB-UGent collection, pEN-2R-P3-GFP. pWOX5:gWOX5-GFP vector was obtained performing multisite Gateway into the destination vector pK7m34GW3. The structure and sequence of all used destination vectors were as described (44, 45). They are accessible on line at http://www.psb.ugent.be/gateway/ or otherwise referenced. All transgenic plants were generated using the floral dip method (46) with Col-0 *Arabidopsis thaliana* line and GV3101 pMP90 Agrobacterium strain.

Growth conditions

Seeds used for confocal microscopy were surface sterilized using fumes produced by a solution of 50% bleach and 1M hydrochloric acid, imbibed and stratified for 2 days at 4°C. After 2 days, the stratified seeds were plated and grown vertically at 22°C in long-day conditions (16-hrs light/ 8-hrs dark) on 1X Murashige and Skoog (MS) medium supplemented with sucrose (1% total). All plant roots were imaged at 5 days after stratification, unless otherwise noted. For the brassinolide (BL) treated plants, Columbia-0 (Col-0), pSHR:SHR:GFP, and pSCR:SCR:GFP seeds were prepared as described above but were plated on ½ MS medium plates with no sucrose and 4 nM Brassinolide. For RNAseq experiments, seeds were wet sterilized using 50% bleach, 100% ethanol, and water. Seeds were imbibed and stratified for 2 days at 4°C. After 2 days, the stratified seeds were plated on Nitex mesh squares on top of 1X MS medium with 1% sucrose. Seeds were plated and grown vertically at 22°C in long-day conditions as described above.

Time course expression of the root meristem

Time course expression of the root meristem was obtained by collecting GFP-negative cells from PET111:GFP (47) lines every 8 hours from 4 days to 6 days post-stratification. Between 100-150mg of seed were wet sterilized and plated (see Growth conditions) for each biological replicate. After growth, approximately 1mm of the root tip was collected and protoplasted as described in (48). GFP negative cells were collected in a solution of beta-mercaptoethanol and RLT buffer using a MoFlo cell sorter. Two to three biological replicates were collected for each time point. RNA was extracted using the Qiagen RNEasy Micro kit. Libraries were prepared using the TruSeq RNA Library Prep Kit v2 from Illumina and sequenced on an Illumina HiSeq 2500 with 100 bp single end reads. Reads were filtered using ea-utils (https://expressionanalysis.github.io/ea-utils/) and mapped using the Tuxedo pipeline (49).

bioRxiv preprint doi: https://doi.org/10.1101/439331; this version posted October 9, 2018. The copyright holder for this preprint (which was not certified by peer review) is the author/funder. All rights reserved. No reuse allowed without permission.

FPKMs were acquired using Cufflinks(49). Raw reads and FPKMs are available from Gene Expression Omnibus (GEO: https://www.ncbi.nlm.nih.gov/geo/), accession #GSE104945).

RNAseq on mutant lines

For the *wox5-1* and *seu-3* RNAseq experiments, approximately 5mm of the root tip was collected. RNA was extracted using the RNeasy Micro Kit (Qiagen). cDNA synthesis and amplification was performed using the NEBNext Ultra II RNA Library Prep Kit for Illumina. Libraries were sequenced on an Illumina HiSeq 2500 with 100 bp single end reads. Reads were filtered and mapped as described in the previous section. Differential expression was calculated using CuffDiff (49) with a cutoff of $q<0.05$ and fold change >2. Raw reads and FPKMs are available from GEO.

Transcriptomic profile of stem and non-stem cells

Between 300-500mg of AGL42:GFP(29) seeds were wet sterilized and plated (see Growth conditions) for each biological replicate. After growth, approximately 1mm of the root tip was collected and protoplasted as described in (48). GFP positive and negative cells were collected in two separate vials containing a solution of beta-mercaptoethanol and RLT buffer using a MoFlo cell sorter. Four biological replicates were collected each for GFP positive and GFP negative cells. RNA was extracted using the Qiagen RNEasy Micro kit. Libraries were prepared using the SMART-Seq v4 Ultra Low RNA Input Kit for Sequencing and the Low Input Library Prep Kit v2 from Clontech. Libraries were sequenced on an Illumina HiSeq 2500 with 100 bp single end reads. Reads were filtered using ea-utils and mapped using RSubread[45]. FPKMs were acquired using Cufflinks (49). Differential expression analysis was performed using PoissonSeq (50) with a cutoff of $q<0.06$ and fold change > 2. Raw reads and FPKMs are available from GEO.

Transcription Factor Yeast Two-Hybrid Assay

The Yeast Two-Hybrid assay was performed as described for the Yeast One-Hybrid assay in (51) with the following modifications. The SEU ORF was cloned into pGBKT7 (Clontech) and transformed into yeast strain AH109. SEU AH109 (bait) and AH109 empty vector were mated to the TF library described in (22) (Supplementary Table 6) and selected on SD-LeuUra. Four independent successful matings were replica-plated to quadruple dropout SD-LeuUraHisAde with and without 100 µg/mL 3-amino-1,2,4-triazol (3AT) and scored for colony growth over a period of four days. Positive interactions were scored as those matings with colony growth on SEU but not empty vector control plates.

qPCR

Total RNA was isolated from approximately 2mm of Col-0, *seu-3 wox5-1*, and *t5l1* root tips using the RNeasy Micro Kit (Qiagen) 5 days after plating. The first strand cDNA was synthesized using the Superscript III First Strand Synthesis Kit (Invitrogen). qPCR was performed with SYBR green (Invitrogen) using a 7500 Fast Real-Time PCR system (Applied

bioRxiv preprint doi: https://doi.org/10.1101/439331; this version posted October 9, 2018. The copyright holder for this preprint (which was not certified by peer review) is the author/funder. All rights reserved. No reuse allowed without permission.

Biosystems) with 40 cycles. Data were analyzed using the ΔΔCt (cycle threshold) method and normalized to the expression of the reference gene UBIQUITIN10 (UBQ10). For each mutant, qPCR was performed on two technical replicates of two independent RNA samples (biological replicates). Results were comparable across biological replicates. Gene-specific primers used are provided in Supplementary Table 13.

Confocal microscopy

Confocal microscopy was completed using a Zeiss LSM 710. Both 488nm and 570nm lasers were used for green and red channel acquisition, respectively. A solution of 10μM propidium iodide was used to stain cell walls for visualization. mPS-PI staining to visualize starch granules was performed as described in(27). For the N&B acquisition, 12-bit raster scans of a 256x256 pixel region of interest were acquired with a pixel size of 100nm and a pixel dwell time of 12.61μs as described in (52). For pCF acquisition, 8-bit line scans of a 32x1 pixel region of interest were acquired with a pixel size range of 40-100nm and a pixel dwell time of 12.61us as described in (52). Heptane glue was used during N&B and pCF acquisition to prevent movement of the sample as described in(52, 53)

Corrected Total Cell Fluorescence (CTCF) Measurements

Corrected Total Cell Fluorescence (CTCF) was calculated to determine the intensity of cells expressing a fluorescently tagged protein. To complete these measurements, the confocal settings (gain, digital offset, laser percentage) were left constant for the entirety of the experiment. Imaging software (ImageJ) was used to measure the CTCF, which is defined as (Integrated density of GFP)/(Area of selected cells * Mean fluorescence of background) where background is a region of the root with no GFP (54). The CTCF was divided by the area of the cells (CTCF/area) before performing statistics to account for different numbers of cells selected in each image. When measuring the CTCF for plants expressing pCYCD6:GUS:GFP, only CEI and CEI daughter cells were used for analysis. When calculating the CTCF of pCYCD6:GUS:GFP expression in *seu-3* and *wox5-1* mutants, there was a wide range in the measured CTCFs. Thus, to compare the samples, CTCF values were separated into three groups, “low” (CTCF/area < 1), “medium” ($1 \leq$ CTCF/area ≤ 5) and “high” values (CTCF/area > 5). The distributions of CTCF values between the samples were then compared using the Chi-Squared Test with Likelihood Ratio.

Number and Brightness (N&B) analysis

Analysis of the raster scans acquired for N&B was performed using the SimFCS software (52, 55)(https://www.lfd.uci.edu/globals/). The 35S:GFP and UBQ10:mCherry lines were used to calibrate software parameters. We used a region of interest of 64x64 or 128x128 pixels to analyze the CEI or QC cells, respectively. The S-factor for GFP (2.85) and for mCherry (0.86) were calculated first to normalize the autofluorescence/background region of the images (Supplementary Figure 15). After the S-factor was set, the monomer brightness of GFP (0.32)

bioRxiv preprint doi: https://doi.org/10.1101/439331; this version posted October 9, 2018. The copyright holder for this preprint (which was not certified by peer review) is the author/funder. All rights reserved. No reuse allowed without permission.

and mCherry (0.26) were measured and found to be similar to what was previously measured in the Arabidopsis root (19) (Supplementary Figure 14). To determine the possible stoichiometries of the SHR-SCR complex, a binding score was determined based on the colors of the stoichiometry histogram (Supplementary Figure 2) where 6 (red) corresponds to the highest amount of binding and 0 (blue) corresponds to no binding.

Pair Correlation Function (pCF) analysis

Analysis of the line scans acquired for pCF was performed using the SimFCS software[49,52] (https://www.lfd.uci.edu/globals/). Three technical replicates (pixel distance = 5, 7, and 9) were analyzed for each image as the cell walls are irregular in size, so changing the pixel distance can result in a different pCF carpet. For each technical replicate, a Movement Index (MI) was assigned based on if movement was detected in the carpet (arch pattern, MI=1) or not (no arch pattern, MI=0) as described in (19, 52). The technical replicates were then averaged for each biological replicate. The WOX5:WOX5:GFP images were analyzed separately in both directions. The 35S:GFP and TMO5:3xGFP control lines were analyzed only in the forward (left to right) direction as it has been previously shown that their movement index does not vary within the stem cell niche(19).

Statistical analysis

All statistical analysis was performed using JMP software (https://www.jmp.com/). The Chi-Squared test with Likelihood ratio was used to determine if there was a significant difference in the distribution of CTCF values of pCYCD6:GUS:GFP expression in *seu-3* and *wox5-1* mutants. For the remainder of the experiments, a Shapiro-Wilk Goodness of Fit test was used to determine normality of the data, and at least one sample in each experiment had a $p<0.05$ for this test, suggesting that not all of the data met normality assumptions. Therefore, the nonparametric equivalents of statistical tests (Wilcoxon test for 2 groups and Wilcoxon test with Steel-Dwass for greater than 2 groups) were used for all remaining statistical comparisons. Two-tailed comparisons were used, and $p<0.05$ was used for significance for all tests. The statistical test used for each experiment is reported in the figure legends. Exact sample sizes are reported in the figure legends and supplementary information. Exact p-values are reported in the supplementary information and in the data repository (see Data Availability).

Mathematical model formulation and simulation

A system of 21 ordinary differential equations (ODEs) was developed to model the dynamics of SHR and SCR in the CEI and QC (see Supplementary Information for equations). Transcriptional regulation is assumed to happen on a fast time scale such that transcriptional and protein dynamics can be modeled in the same equation. Transcriptional regulation is modeled using Hill equation dynamics, and SHR-SCR complex formation is modeled using mass-action kinetics. SHR diffusion is modeled using a linear term for gradient-independent diffusion. All proteins are assumed to have a linear degradation term. All 4 stoichiometries of the SHR-SCR

bioRxiv preprint doi: https://doi.org/10.1101/439331; this version posted October 9, 2018. The copyright holder for this preprint (which was not certified by peer review) is the author/funder. All rights reserved. No reuse allowed without permission.

complex are assumed to activate SCR (17, 19), and it is also assumed that SCR can activate itself (8, 17).

The second version of the model incorporates a Hill equation modeling the regulation of SHR by its activator and repressor. It is assumed that the regulation operates in an "OR" gate such that if the activator and repressor both bind the SHR promoter, the activator overcomes the repressor. This is based on results showing that SHR activator mutants have root phenotypes while SHR repressor mutants do not, suggesting that the activator is stronger than the repressor (22). Another Hill equation models the regulation of SCR by a repressor and the SHR-SCR complex. Finally, the production terms for the SHR activator, SHR repressor, and SCR repressor are assumed to be time-dependent as this produces the best model fit to the experimental data. MATLAB code containing the ODE model is included on figshare (see Data Availability).

Given the experimental results that the CEI divides at 5D, but the QC does not divide at 5D (Figures 3B, 4B), the model was simulated for 4D-5D and 5D-6D separately. To simulate division of the CEI, model values for all of the proteins present in the CEI at 5D were divided by 2. These halved values were then used as the initial values for 5D-6D. It was also assumed that the vasculature divides at 5D, so the same process was repeated for proteins in the vasculature. Since the QC does not divide, protein values in the QC at 5D were used as the initial values for 5D-6D. The model simulations from 4D-5D and 5D-6D were then combined to form the final simulations seen in Figures 1,3, and 4. MATLAB code used to run these simulations is included on figshare (see Data Availability).

Sensitivity analysis of mathematical model

Sensitivity analysis was performed on a version of the model that does not incorporate the QC as the equations for all of the proteins in the CEI and QC are the same: therefore, the sensitivity index of the parameters will be the same in both cell types. The total Sobol effect index (19, 56, 57) was calculated for each parameter value. Parameter values were randomly sampled using Monte Carlo sampling to obtain 150 different values for each parameter (Supplementary Table 10). This process was repeated for 10 technical replicates. The sample number was chosen as 150 as this makes the runtime of the sensitivity analysis approximately 2 hours per technical replicate on an Intel i7-4800MQ 2.70 GHz CPU with 8GB RAM. MATLAB code for calculating the total Sobol index is included on figshare (see Data Availability). The sensitivity of each variable to each parameter was normalized to [0,1] and then averaged to calculate the final sensitivity indices. The sensitive parameters were chosen as the parameters that had significantly higher Sobol indices than the selected cutoff parameter (k_6) using the Wilcoxon test with Steel-Dwass for multiple comparisons with a significance cutoff of $p<0.05$.

Parameter estimation

bioRxiv preprint doi: https://doi.org/10.1101/439331; this version posted October 9, 2018. The copyright holder for this preprint (which was not certified by peer review) is the author/funder. All rights reserved. No reuse allowed without permission.

The initial values for S_v (SHR monomer in vasculature), C_e (SCR monomer in CEI), and C_q (SCR monomer in QC) were determined using the FPKM values for SHR and SCR at 4D from replicate 1 of the time course dataset. Since SCR is expressed in both the CEI and QC, the FPKM value needed to be split between the two cells. To accomplish this, expression of SCR was obtained from a dataset of Arabidopsis root tissues (28). It was determined that 41.91% of SCR is expressed in the QC, while the remaining 58.09% is expressed in the CEI and endodermis (Supplementary Table 11). In addition, the results from the N&B analysis (Figure 1) were used to set the initial value of C_{2q} (SCR dimer in the QC). Once SEU and WOX5 were incorporated into the model, their FPKM values at 4D were used for the initial conditions for X (SHR activator) and Y (SHR repressor), respectively (Supplementary Table 3).

For the production rate of SHR dimer in the CEI and QC (k_{2e} and k_{2q}, respectively), the FPKM values of SCR were used to determine the value for C_0, which is the concentration of SCR at which SHR dimer begins to form. It was assumed that the concentration of SCR required for SHR dimer formation is the same in both the CEI and QC. The value of SCR at 4D 16H (FPKM of 10.04) was taken as the steady state value because after this time SCR levels began to decrease. This value was then divided by 2 based on the assumption that C_0, should be the same value in the CEI and QC (FPKM of 5.02 in each cell). Finally, this value was multiplied by 0.6 as previous results show that SHR dimer can form when SCR is at least 60% of its steady state levels(17), resulting in the value C_0=3. The steepness of the function, s, was chosen such that the production of SHR dimer reaches its maximum value as soon as SCR levels exceed C_0 (as detailed in[23]). Thus, estimating k_{2e} and k_{2q} boiled down to estimating L_e and L_q, which are the maximum values for k_{2e} and k_{2q} in the CEI and QC, respectively.

The parameters involved in SCR dimer formation in the CEI were set to 0 as the SCR dimer is at very low levels in the CEI (Supplementary Figure 1). Additionally, the diffusion coefficients of SHR (a_e, a_q) were not estimated as they were experimentally determined from RICS experiments in (19). The remaining sensitive parameters except for k_1, k_{3e}, and k_{3q} were set to constant values using the N&B data measured at 5D (Supplementary Table 3).

k_1, k_{3e} and k_{3q} were estimated from the time course of the root meristem using simulated annealing (58). The residual function to calculate the model error uses FPKM values for SHR and SCR from replicate 1 of the time course. Latin hypercube sampling was used to sample the parameter space (defined in Supplementary Table 3) for a total of 50 sets of initial parameter estimates. Each set of initial estimates was fit to the residual function using simulated annealing with least squares (simulannealbnd function in MATLAB) for 5 minutes (total runtime = 250 minutes for 50 sets of initial estimates). Thirty-three parameter sets that did not converge were removed, leaving 17 total estimated parameter sets (Supplementary Figure 2, Supplementary Table 12). The average of these parameter values was used in the final model simulation

bioRxiv preprint doi: https://doi.org/10.1101/439331; this version posted October 9, 2018. The copyright holder for this preprint (which was not certified by peer review) is the author/funder. All rights reserved. No reuse allowed without permission.

(Supplementary Table 12). MATLAB code used for simulated annealing is included on figshare (see Data Availability).

Finally, the production terms for the SHR activator, SHR repressor, and SCR repressor (k_9, k_{10}, and k_{11e} and k_{11q} respectively) were set to a constant value at each time point based to minimize the model error compared to the time course data. Once SEU and WOX5 were identified as the SHR activator and repressor, k_9 and k_{10} were re-estimated to minimize the error between the model and the time course expression data for these genes (Supplementary Table 10)

Sign score calculation

The sign score was used to compare the time course expression of candidate genes with the mathematical model prediction. The time course expression for the predicted SHR activators and repressors was obtained from the RNAseq time course of the root meristem. Replicate 1 was used for all of the candidate genes as only this replicate shows coexpression of SHR and SCR over time, which is supported by experimental evidence that SHR and SCR activate SCR expression[13]. The sign score of the gene candidates compared to the model prediction was then calculated. The sign score is defined as the change in the model prediction between two time points (+1 for positive change, 0 for zero change, and -1 for negative change) times the change in the gene time course expression between the same two time points. Thus, the genes with a temporal pattern that is exactly the same as the model prediction will have the maximum possible sign score of 5. A threshold of 1.1 was used to determine a change in expression, meaning that gene expression must change at least 1.1-fold between time points in order to be recorded as a positive or negative change.

Data availability

All raw images and data, as well as all MATLAB code used for the model, are available on figshare: 10.6084/m9.figshare.c.4259609

Acknowledgements

We thank Erin Sparks, Cara Winter, and Philip Benfey for their insightful comments on this manuscript.

Funding

This work was supported by a NSF GRF (DGE-1252376) awarded to NMC and APF. Research in R. Simon lab was funded by the DFG through Si947/10 and an AvH fellowship for BB. SGZ was supported by the Howard Hughes Medical Institute and by a grant from the National Institute of Health (NIH) (GM118036). R. Sozzani and NMC are supported by a NSF CAREER grant (MCB-1453130).

bioRxiv preprint doi: https://doi.org/10.1101/439331; this version posted October 9, 2018. The copyright holder for this preprint (which was not certified by peer review) is the author/funder. All rights reserved. No reuse allowed without permission.

References

1. Fisher AP, Sozzani R (2016) Uncovering the networks involved in stem cell maintenance and asymmetric cell division in the Arabidopsis root. *Curr Opin Plant Biol* 29:38–43.
2. Heidstra R, Sabatini S (2014) Plant and animal stem cells: Similar yet different. *Nat Rev Mol Cell Biol* 15(5):301–312.
3. Gallagher KL, Paquette AJ, Nakajima K, Benfey PN (2004) Mechanisms Regulating SHORT-ROOT Intercellular Movement. *Curr Biol* 14:1847–1851.
4. Pi L, et al. (2015) Organizer-Derived WOX5 Signal Maintains Root Columella Stem Cells through Chromatin-Mediated Repression of CDF4 Expression. *Dev Cell* 33(5):576–588.
5. Gallagher KL, Benfey PN (2005) Not just another hole in the wall: Understanding intercellular protein trafficking. *Genes Dev* 19(2):189–195.
6. Levesque MP, et al. (2006) Whole-genome analysis of the SHORT-ROOT developmental pathway in Arabidopsis. *PLoS Biol* 4(5):e143.
7. Sozzani R, et al. (2010) Spatiotemporal regulation of cell-cycle genes by SHORTROOT links patterning and growth. *Nature* 466:128–132.
8. Cruz-Ramírez A, et al. (2012) A bistable circuit involving SCARECROW-RETINOBLASTOMA integrates cues to inform asymmetric stem cell division. *Cell* 150(5):1002–1015.
9. Long Y, et al. (2017) In vivo FRET-FLIM reveals cell-type-specific protein interactions in Arabidopsis roots. *Nature* 548(7665):97–102.
10. Gallagher KL, Benfey PN (2009) Both the conserved GRAS domain and nuclear localization are required for SHORT-ROOT movement. *Plant J* 57:785–797.
11. Helariutta Y, et al. (2000) The SHORT-ROOT Gene Controls Radial Patterning of the Arabidopsis Root through Radial Signaling. *Cell* 101:555–567.
12. Nakajima K, Sena G, Nawy T, Benfey PN (2001) Intercellular movement of the putative transcription factor SHR in root patterning. *Nature* 413(6853):307–311.
13. Koizumi K, Hayashi T, Wu S, Gallagher KL (2012) The SHORT-ROOT protein acts as a mobile, dose-dependent signal in patterning the ground tissue. *Proc Natl Acad Sci* 109(32):13010–13015.
14. Long Y, et al. (2015) Arabidopsis BIRD Zinc Finger Proteins Jointly Stabilize Tissue Boundaries by Confi ning the Cell Fate Regulator SHORT-ROOT and Contributing to Fate Specifi cation. *Plant Cell* 27:1185–1199.
15. Moreno-Risueno MA, et al. (2015) Transcriptional control of tissue formation throughout root development. *Science (80-)* 350(6259):426–430.
16. Welch D, et al. (2007) Arabidopsis JACKDAW and MAGPIE zinc finger proteins delimit asymmetric cell division and stabilize tissue boundaries by restricting SHORT-ROOT action. *Genes Dev* 21(17):2196–2204.
17. Cui H, et al. (2007) An Evolutionarily Conserved Mechanism Delimiting SHR Movement Defines a Single Layer of Endodermis in Plants. *Science (80-)* 316:421–425.
18. Koizumi K, Hayashi T, Gallagher KL (2012) SCARECROW reinforces SHORT-ROOT signaling and inhibits periclinal cell divisions in the ground tissue by maintaining SHR at high levels in the endodermis. *Plant Signal Behav* 7(12):1573–1577.
19. Clark NM, et al. (2016) Tracking transcription factor mobility and interaction in Arabidopsis roots with fluorescence correlation spectroscopy. *Elife* 5:e14770.
20. Nakashima K, Takasaki H, Mizoi J (2012) NAC transcription factors in plant abiotic

bioRxiv preprint doi: https://doi.org/10.1101/439331; this version posted October 9, 2018. The copyright holder for this preprint (which was not certified by peer review) is the author/funder. All rights reserved. No reuse allowed without permission.

stress responses. *Biochim Biphysica Acta* 1819:97–103.
21. Chen YF, et al. (2010) Ethylene receptors function as components of high-molecular-mass protein complexes in Arabidopsis. *PLoS One* 5(1). doi:10.1371/journal.pone.0008640.
22. Sparks EE, et al. (2016) Establishment of Expression in the SHORTROOT-SCARECROW Transcriptional Cascade through Opposing Activities of Both Activators and Repressors. *Dev Cell* 39(5):585–596.
23. Brady SM, et al. (2011) A stele-enriched gene regulatory network in the Arabidopsis root. *Mol Syst Biol* 7(459):1–9.
24. Aichinger E, Villar CBR, Di Mambro R, Sabatini S, Kohler C (2011) The CHD3 Chromatin Remodeler PICKLE and Polycomb Group Proteins Antagonistically Regulate Meristem Activity in the Arabidopsis Root. *Plant Cell* 23(3):1047–1060.
25. Gong X, et al. (2016) SEUSS integrates gibberellin signaling with transcriptional inputs from the SHR-SCR-SCL3 module to regulate middle cortex formation in the Arabidopsis root. *Plant Physiol* 170:pp.01501.2015.
26. Sridhar V V., Surendrarao A, Gonzalez D, Conlan RS, Liu Z (2004) Transcriptional repression of target genes by LEUNIG and SEUSS, two interacting regulatory proteins for Arabidopsis flower development. *Proc Natl Acad Sci* 101(31):11494–11499.
27. de Luis Balaguer MA, et al. (2017) Predicting gene regulatory networks by combining spatial and temporal gene expression data in *Arabidopsis* root stem cells. *Proc Natl Acad Sci* 114(36):E7632–E7640.
28. Li S, Yamada M, Han X, Ohler U, Benfey PN (2016) High-Resolution Expression Map of the Arabidopsis Root Reveals Alternative Splicing and lincRNA Regulation. *Dev Cell* 39(4):508–522.
29. Nawy T, et al. (2005) Transcriptional Pro le of the Arabidopsis Root Quiescent Center. *Plant Cell* 17:1908–1925.
30. Sarkar AK, et al. (2007) Conserved factors regulate signalling in Arabidopsis thaliana shoot and root stem cell organizers. *Nature* 446(7137):811–814.
31. Stahl Y, Wink RH, Ingram GC, Simon R (2009) A Signaling Module Controlling the Stem Cell Niche in Arabidopsis Root Meristems. *Curr Biol* 19(11):909–914.
32. Cruz-Ramírez A, et al. (2013) A SCARECROW-RETINOBLASTOMA Protein Network Controls Protective Quiescence in the Arabidopsis Root Stem Cell Organizer. *PLoS Biol* 11(11):e1001724.
33. Vilarrasa-Blasi J, et al. (2014) Regulation of plant stem cell quiescence by a brassinosteroid signaling module. *Dev Cell* 30(1):36–47.
34. Stahl Y, et al. (2013) Moderation of arabidopsis root stemness by CLAVATA1 and ARABIDOPSIS CRINKLY4 receptor kinase complexes. *Curr Biol* 23(5):362–371.
35. Sabatini S, Heidstra R, Wildwater M, Scheres B (2003) SCARECROW is involved in positioning the stem cell niche in the Arabidopsis root meristem. *Genes Dev*:354–358.
36. Gonzalez-Garcia M-P, et al. (2011) Brassinosteroids control meristem size by promoting cell cycle progression in Arabidopsis roots. *Development* 138(5):849–859.
37. Forzani C, et al. (2014) WOX5 suppresses CYCLIN D activity to establish quiescence at the Center of the root stem cell niche. *Curr Biol* 24(16):1939–1944.
38. Vanstraelen M, et al. (2009) APC/C ^{CCS52A} complexes control meristem maintenance in the *Arabidopsis* root. *Proc Natl Acad Sci* 106(28):11806–11811.
39. Heyman J, et al. (2013) ERF115 controls root quiescent center cell division and stem cell replenishment. *Science* 342(6160):860–863.

bioRxiv preprint doi: https://doi.org/10.1101/439331; this version posted October 9, 2018. The copyright holder for this preprint (which was not certified by peer review) is the author/funder. All rights reserved. No reuse allowed without permission.

40. Wendrich JR, et al. (2017) Framework for gradual progression of cell ontogeny in the *Arabidopsis* root meristem. *Proc Natl Acad Sci* 114(42):E8922–E8929.
41. Bao F, Azhakanandam S, Franks RG (2010) SEUSS and SEUSS-LIKE Transcriptional Adaptors Regulate Floral and Embryonic Development in Arabidopsis. *Plant Physiol* 152(2):821–836.
42. De Rybel B, et al. (2013) A bHLH Complex Controls Embryonic Vascular Tissue Establishment and Indeterminate Growth in Arabidopsis. *Dev Cell* 24:426–437.
43. Azhakanandam S, Nole-Wilson S, Bao F, Franks RG (2008) SEUSS and AINTEGUMENTA Mediate Patterning and Ovule Initiation during Gynoecium Medial Domain Development. *Plant Physiol* 146(3):1165–1181.
44. Karimi M, Inze D, Depicker A (2002) GATEWAY vectors for Agrobacterium-mediated plant transformation. *Trends Plant Sci* 7(5):193–195.
45. Karimi M, Depicker A, Hilson P (2007) Recombinational Cloning with Plant Gateway Vectors. *Plant Physiol* 145(4):1144–1154.
46. Clough SJ, Bent AF (1998) Floral dip: A simplified method for Agrobacterium-mediated transformation of *Arabidopsis thaliana*. *Plant J* 16(6):735–743.
47. Brady SM, et al. (2007) A High-Resolution Root Spatiotemporal Map Reveals Dominant Expression Patterns. *Science* 318:801–806.
48. Birnbaum K, et al. (2005) Cell type-specific expression profiling in plants via cell sorting of protoplasts from fluorescent reporter lines. *Nat Methods* 2(8):615–619.
49. Trapnell C, et al. (2012) Differential gene and transcript expression analysis of RNA-seq experiments with TopHat and Cufflinks. *Nat Protoc* 7(3):562–78.
50. Li J, Witten DM, Johnstone IM, Tibshirani R (2012) Normalization, testing, and false discovery rate estimation for RNA-sequencing data. *Biostatistics* 13(3):523–538.
51. Sparks EE, Benfey PN (2016) Identifying Gene Regulatory Networks in Arabidopsis by In Silico Prediction, Yeast-1-Hybrid, and Inducible Gene Profiling Assays. *Plant Cell Division: Methods and Protocols*, pp 29–50.
52. Clark NM, Sozzani R (2017) Measuring Protein Movement, Oligomerization State, and Protein–Protein Interaction in Arabidopsis Roots Using Scanning Fluorescence Correlation Spectroscopy (Scanning FCS). *Plant Genomics: Methods and Protocols*, pp 251–266.
53. Supatto W, Mcmahon A, Fraser S, Stathopoulos A (2009) Quantitative imaging of collective cell migration during Drosophila gastrulation: multiphoton microscopy and computational analysis. *Nat Protoc* 4(10):1397–1412.
54. McCloy RA, et al. (2014) Partial inhibition of Cdk1 in G2phase overrides the SAC and decouples mitotic events. *Cell Cycle* 13(9):1400–1412.
55. Digman MA, et al. (2005) Measuring Fast Dynamics in Solutions and Cells with a Laser Scanning Microscope. *Biophys J* 89(2):1317–1327.
56. Sobol IM (2001) Global sensitivity indices for nonlinear mathematical models and their Monte Carlo estimates. *Math Comput Simul* 55(1–3):271–280.
57. Saltelli A, et al. (2010) Variance based sensitivity analysis of model output . Design and estimator for the total sensitivity index. *Comput Phys Commun* 181(2):259–270.
58. Kirkpatrick S (1984) Optimization by simulated annealing: Quantitative studies. *J Stat Phys* 34:975–986.

bioRxiv preprint doi: https://doi.org/10.1101/439331; this version posted October 9, 2018. The copyright holder for this preprint (which was not certified by peer review) is the author/funder. All rights reserved. No reuse allowed without permission.

Main Figures

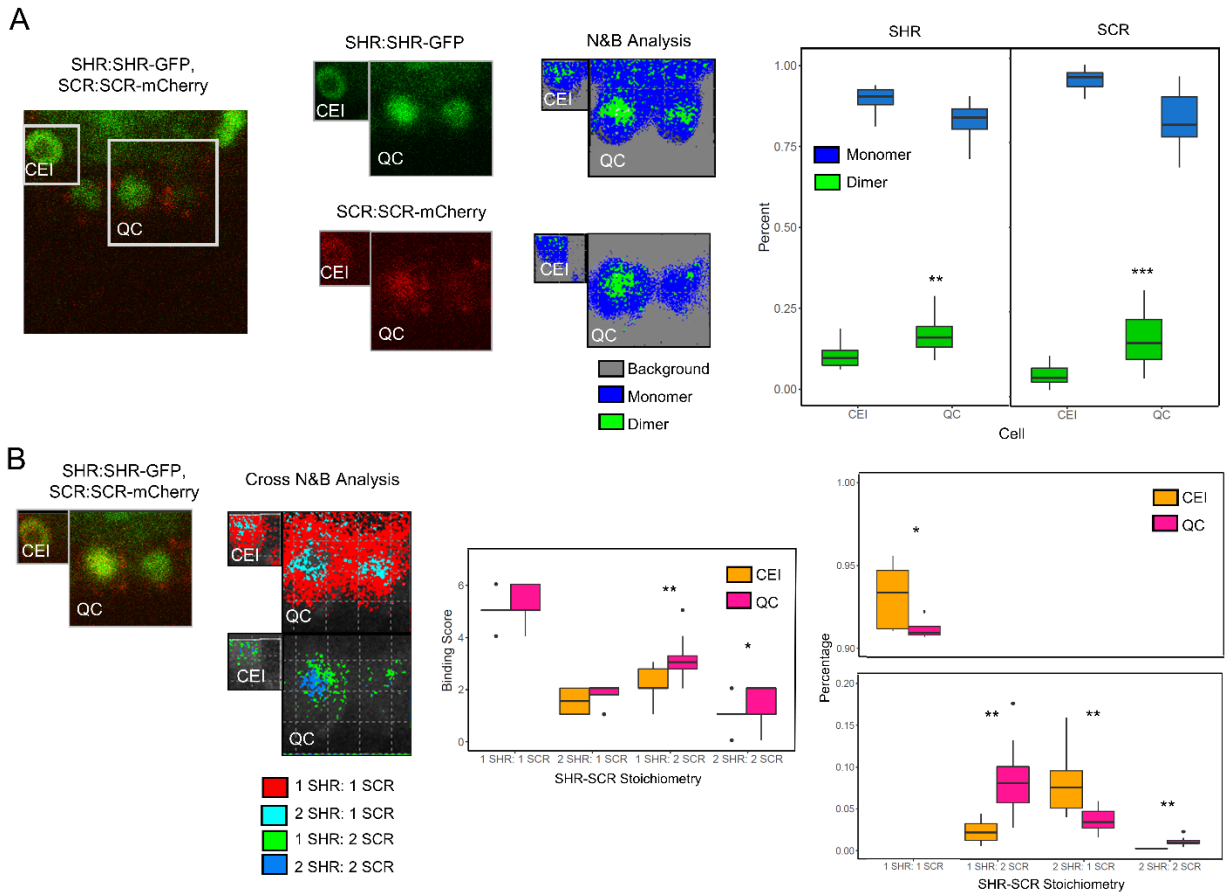

Figure 1: SHR-SCR oligomeric state and stoichiometry differs between CEI and QC. (A) (left) Representative image of SHR:SHR-GFP, SCR:SCR-mCherry in the stem cell niche. Boxes show ROI used for analysis (middle left) SHR:SHR-GFP (top) and SCR:SCR-mCherry (bottom) in the QC (left) and CEI (right). (middle right) N&B analysis of images on the left. Grey represents background fluorescence, blue monomer, and green dimer. (right) Quantification of oligomeric state of SHR (left, n=15) and SCR (right, n=14). ** denotes $p < 0.05$, *** denotes $p < 0.01$, Wilcoxon test. (B) (left) Representative image of SHR:SHR-GFP, SCR:SCR-mCherry in the QC (left) and CEI (right). (second from left) Cross N&B analysis of image on the left. Red represents 1 SHR: 1 SCR, light blue represents 2 SHR: 1 SCR, green represents 1 SHR: 2 SCR, and dark blue represents 2 SHR: 2SCR complex. (third from left) Quantification of complex binding scores in the CEI (orange, n=12) and QC (purple, n=12). (right) Quantification of the percentage of SHR-SCR complex stoichiometries in the CEI (orange, n=12) and QC (pink, n=12). There is a break in the graph from 0.2 to 0.9. ** denotes $p < 0.05$, * denotes $p < 0.1$, Wilcoxon test.

bioRxiv preprint doi: https://doi.org/10.1101/439331; this version posted October 9, 2018. The copyright holder for this preprint (which was not certified by peer review) is the author/funder. All rights reserved. No reuse allowed without permission.

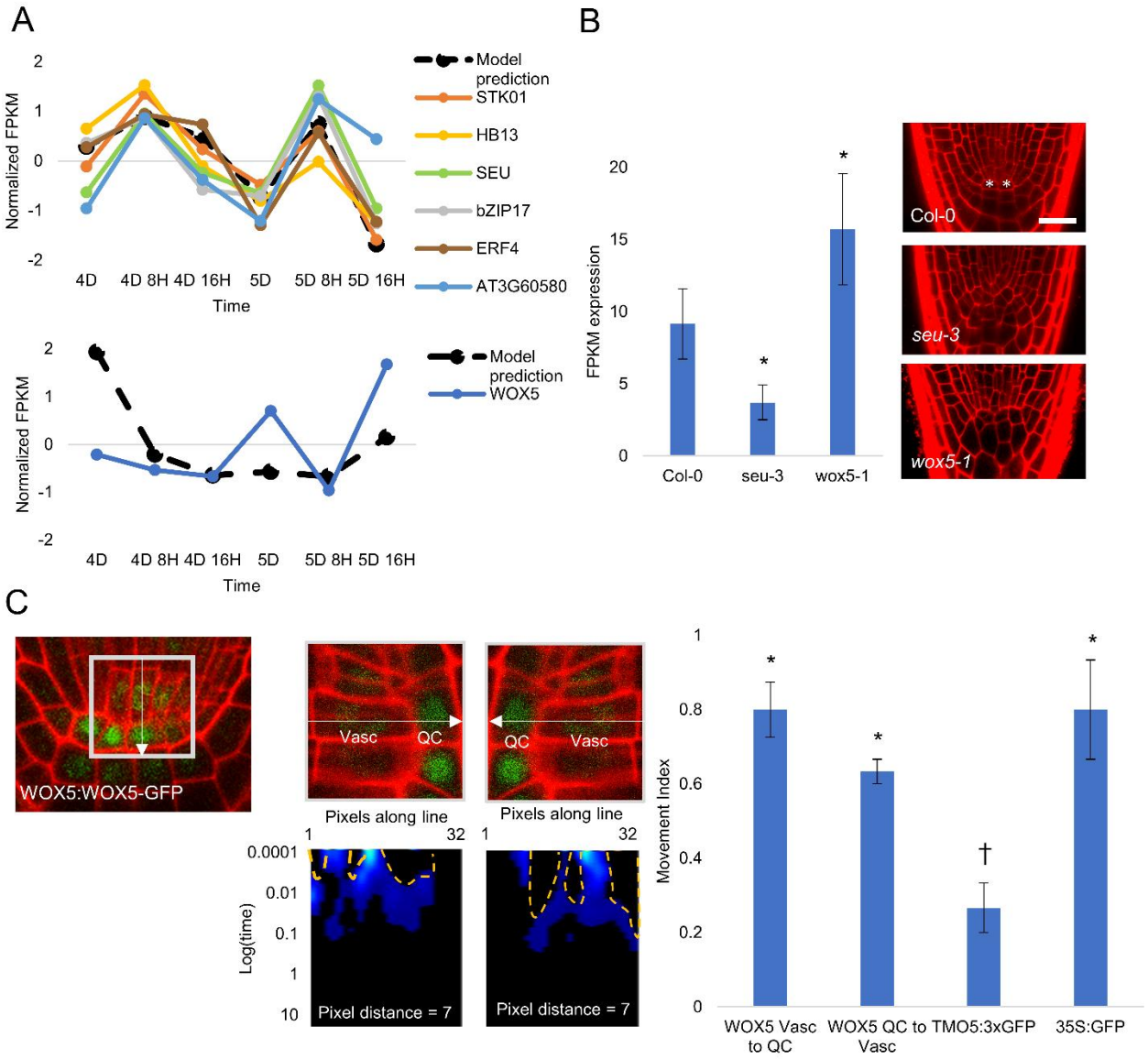

Figure 2: Model prediction and transcriptional profiling identify putative SHR activator and repressor. (A) Black, dashed line indicates the normalized FPKM value of a SHR activator (top) and SHR repressor (bottom) as predicted by the model using the time course dataset. Colored lines represent the normalized FPKM value of the genes with the maximum possible sign score (i.e. best candidates) (B) (left) SHR expression in *seu-3* and *wox5*-1 mutants. * denotes q < 0.05 and fold change > 2 vs Col-0 (Cuffdiff). Error bars represent 95% confidence intervals returned by Cuffdiff. (right) Confocal images showing wild-type root stem cell niche (top), *seu-3* and *wox5*-1 mutant roots with disorganized stem cell niche (middle, bottom). * denotes QC cells in wild-type root. Scale bar = 20 µm. (C) (left) Image of WOX5:WOX5-GFP root showing the location and direction of the line scan. (middle, top) Representative image of WOX5:WOX5:GFP line used for pCF with Quiescent Center (QC) and Vasculature (Vasc) marked. White line shows direction of movement tested. (middle, bottom) pCF carpet of the top panel images. Orange, dashed regions represent arches in the pCF carpet, which denote

bioRxiv preprint doi: https://doi.org/10.1101/439331; this version posted October 9, 2018. The copyright holder for this preprint (which was not certified by peer review) is the author/funder. All rights reserved. No reuse allowed without permission.

movement. (Right) Movement index of WOX5:WOX5:GFP (n=10), an immobile control (TMO5:GFP, n=5), and a mobile control (35S:GFP, n=5) between the QC and vasculature. * denotes p<0.05 as compared to non-mobile control using Wilcoxon with Steel Dwass. Error bars are SEM.

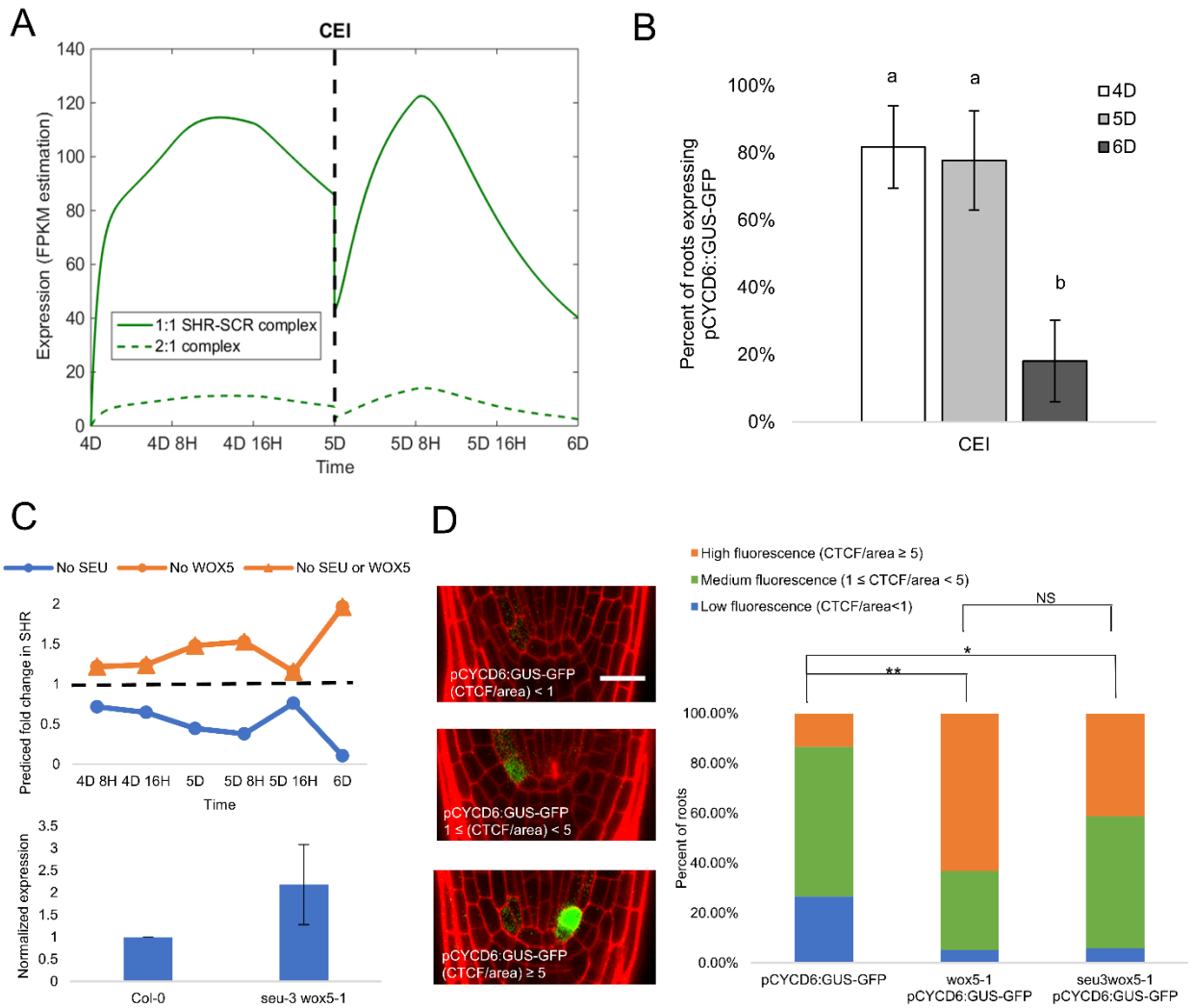

Figure 3: Model predicts timing of CEI divisions

(A) Model simulation of the expression of SHR/SCR complexes in the endodermis. Black dashed line demarcates CEI division at 5D. Green, solid line represents 1 SHR: 1 SCR complex. Green, dashed line represents 2 SHR: 1 SCR complex. (B) Observed changes in the percent of roots expressing pCYCD6::GUS-GFP (white bar, n=11 at 4D. Light gray bar, n=9 at 5D. Dark gray bar, n=11 at 6D). a denotes p < 0.05 compared to b, Steel-Dwass for multiple comparisons. Error bars are SEM. (C) (top) Model prediction of fold change in SHR expression in different mutant backgrounds. Blue line represents no SEU production. Orange line represents no WOX5 production. Orange line with triangles represents no SEU or WOX5 production. Black, dashed line indicates a fold-change of 1, where the expression would be equal to the wild type model

bioRxiv preprint doi: https://doi.org/10.1101/439331; this version posted October 9, 2018. The copyright holder for this preprint (which was not certified by peer review) is the author/funder. All rights reserved. No reuse allowed without permission.

prediction. (bottom) SHR expression in *seu-3 wox5-1* mutants measured using qPCR. Results are from two biological replicates. (D) (left) Representative images of CYCD6::GUS-GFP with low fluorescence (CTCF/area) < 1, medium fluorescence 1 < (CTCF/area) < 5, high fluorescence (CTCF/area) > 5 (right half). Scale bar = 20 µm. (right) Quantification of CYCD6:GUS-GFP expression in wild-type (Col-0, n=15), *wox5-1* (n=19), and *seu-3;wox5-1* (n=17) lines. Blue part of bar represents low fluorescence. Green part of bar represents medium fluorescence. Orange part of bar represents high fluorescence. ** denotes $p < 0.05$, * denotes $p < 0.1$, NS denotes not significant, Chi-squared test with likelihood ratio.

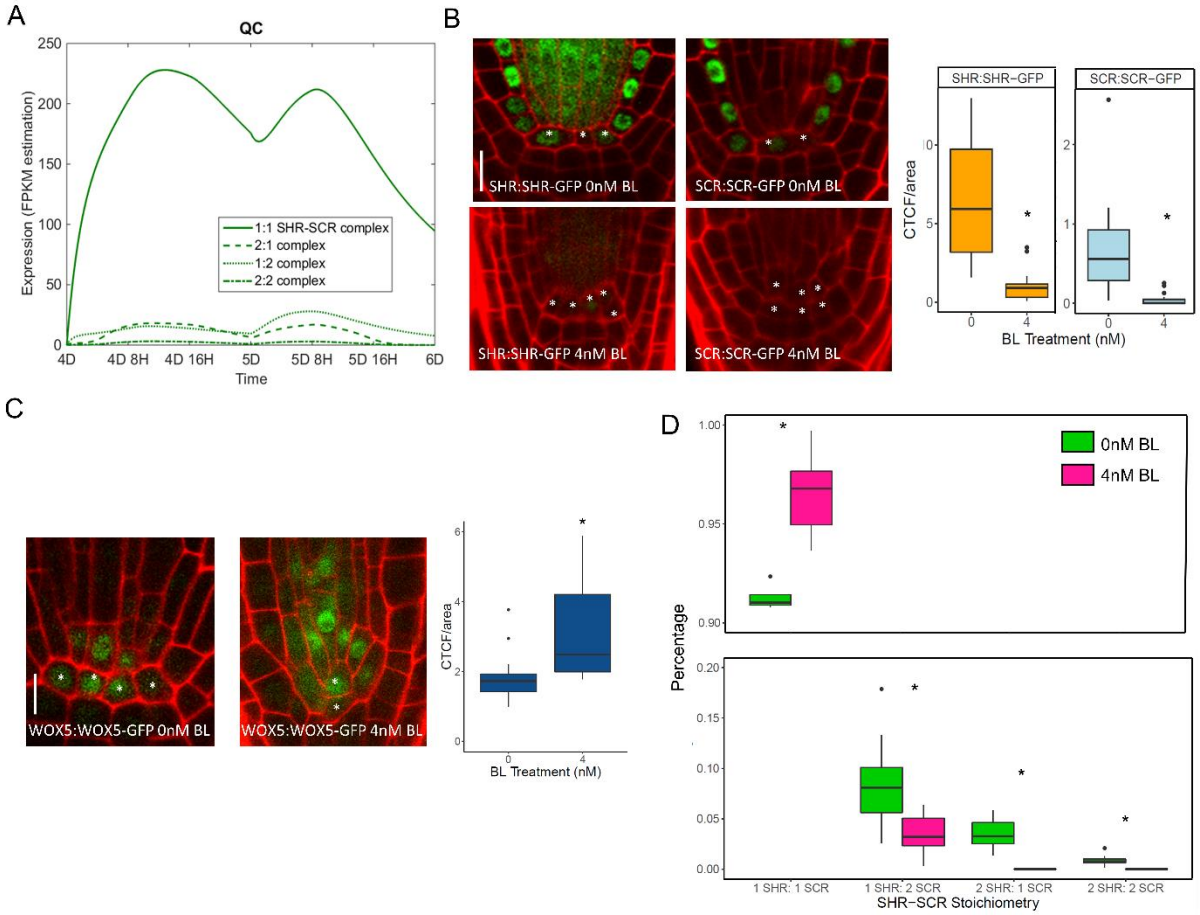

Figure 4: QC division correlates with reduced SHR and SCR accumulation, increased WOX5 accumulation, and a change in SHR-SCR stoichiometry formation.

(A) Model simulation of the expression of SHR/SCR complexes in the QC. Green solid line represents 1 SHR: 1 SCR. Green dashed line represents 2 SHR: 1 SCR. Green dotted line represents 1 SHR: 2 SCR. Green dot/dashed line represents 2 SHR: 1 SCR. (B) (Left) Representative images of 5 day old SHR:SHR-GFP (top half) or SCR:SCR-GFP (bottom half) with or without 4nM BL. * denotes QC cells. Scale bar = 10 µm. (Right) Corrected total cell fluorescence (CTCF) of SHR:SHR-GFP (n=18) and SCR:SCR-GFP (n=16) in 0 and 4 nM BL treated plants. Black dots represent outliers. * denotes $p < 0.05$, Wilcoxon Test. (C) Representative images of WOX5:WOX5-GFP grown in 0nM (left) and 4nM (right) BL. *

bioRxiv preprint doi: https://doi.org/10.1101/439331; this version posted October 9, 2018. The copyright holder for this preprint (which was not certified by peer review) is the author/funder. All rights reserved. No reuse allowed without permission.

denotes QC cells. Scale bar = 10 µm (right) CTCF of WOX5:WOX5-GFP in 0nM (n=13) and 4nM (n=9) BL. * denotes p<0.05, Wilcoxon test. (D) Proportion of SHR-SCR stoichiometries in the QC of plants grown in 0nM (green) and 4nM (pink) BL. * denotes p < 0.05, Wilcoxon test.

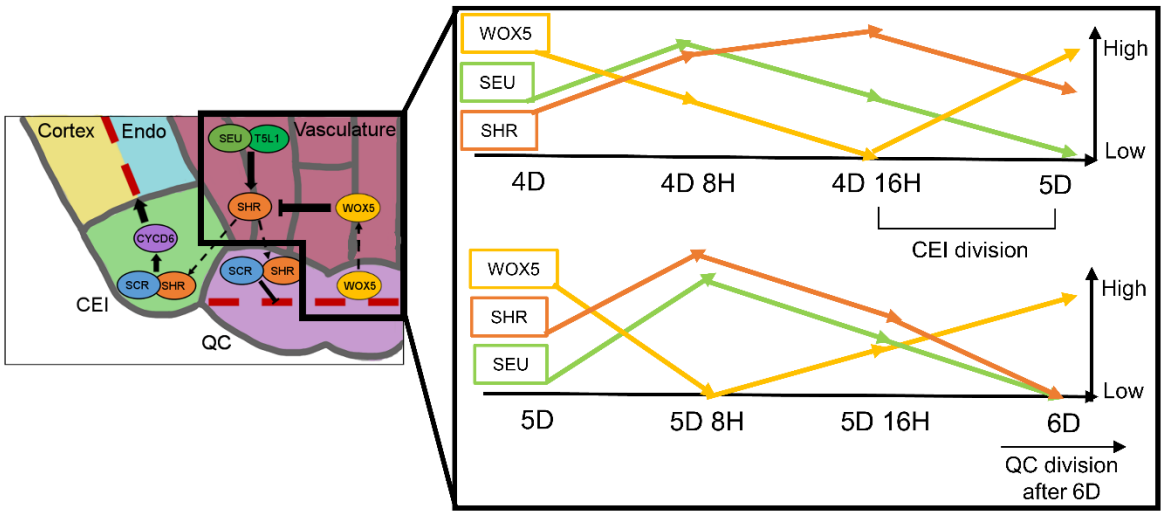

Figure 5: A SEU-WOX5-SHR-SCR network controls timing of CEI and QC division
(Right) Schematic of the Arabidopsis root stem cell niche. SHR protein (orange) moves from the vasculature into the CEI and QC, where it binds SCR. In the CEI, SHR-SCR activates CYCD6 to promote the periclinal division of the CEI daughter (red, dashed line). In the QC, SHR-SCR represses QC division (red, dashed line). WOX5 protein (yellow) moves from the QC to the vasculature to repress SHR. SEU protein (light green) and its binding partner T5L1 (dark green) activate SHR in the vasculature. (Left, inset) Protein dynamics in the vasculature. The combined activation and repression of WOX5 and SEU, respectively, causes temporal changes in SHR expression. High SHR expression between 4D 16H and 5D coordinates the periclinal division of the CEI daughter. Low SHR expression at 6D correlates with QC division sometime after 6D.

bioRxiv preprint doi: https://doi.org/10.1101/439331; this version posted October 9, 2018. The copyright holder for this preprint (which was not certified by peer review) is the author/funder. All rights reserved. No reuse allowed without permission.

Supplementary Figures

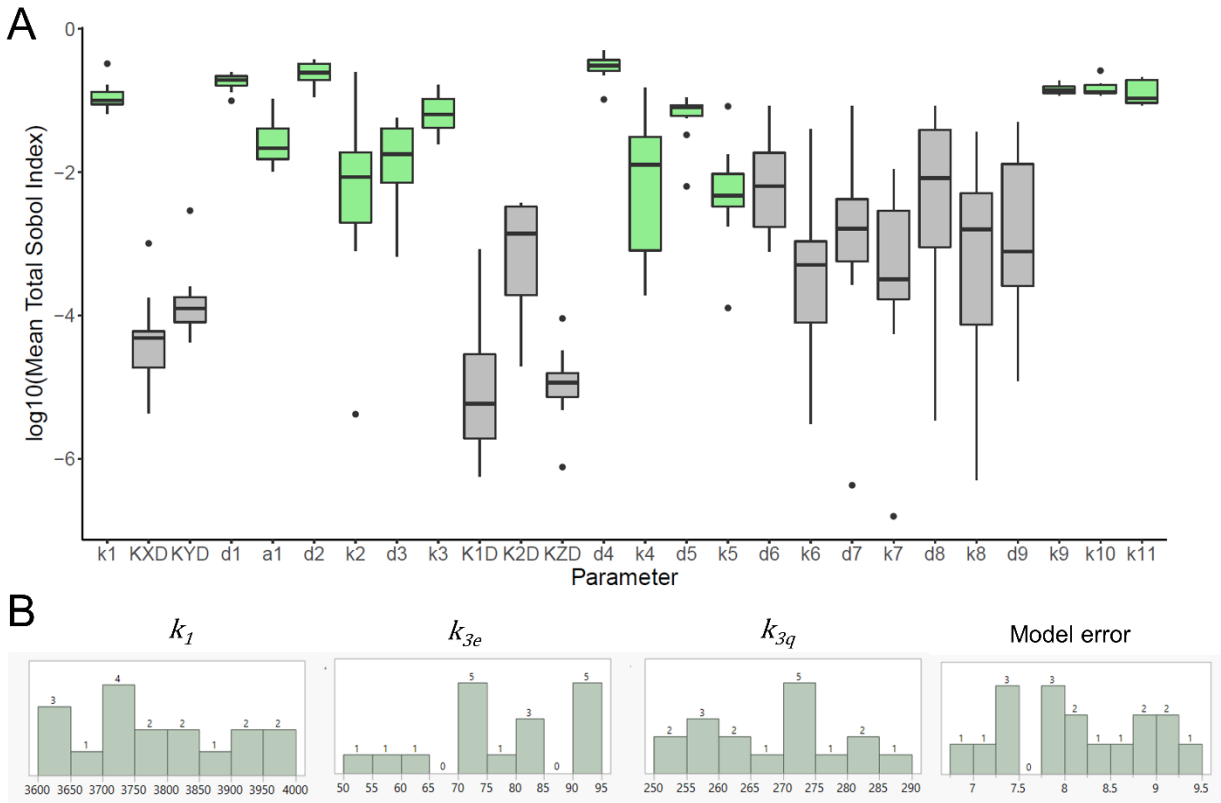

Supplementary Figure 1: Sensitivity analysis and parameter estimation for SHR-SCR model. (A) Sensitivity analysis of SHR-SCR model. The Total Sobol Index was calculated for 10 technical replicates. The y-axis is displayed in a log10 scale. Green parameters are significantly sensitivity compared to k_6, $p<0.05$, Wilcoxon with Steel Dwass. (B) Parameter estimation of SHR monomer production (k_1) and SCR monomer production (k_{3e}, k_{3q}) from time course dataset. The distribution of 17 best-fitting parameter sets is shown along with the model error for each set (far right histogram). Numbers above each bar represent the number of parameter sets in that range.

bioRxiv preprint doi: https://doi.org/10.1101/439331; this version posted October 9, 2018. The copyright holder for this preprint (which was not certified by peer review) is the author/funder. All rights reserved. No reuse allowed without permission.

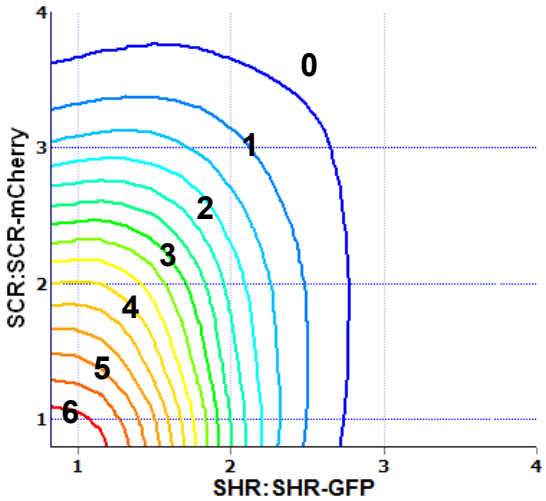

Supplemental Figure 2: Binding score for cross N&B analysis. Numbers correspond to the binding score given to complex stoichiometries depending on the color of the line in the stoichiometry plot. For example, red lines correspond to a score of 6, orange lines to 5, and so on.

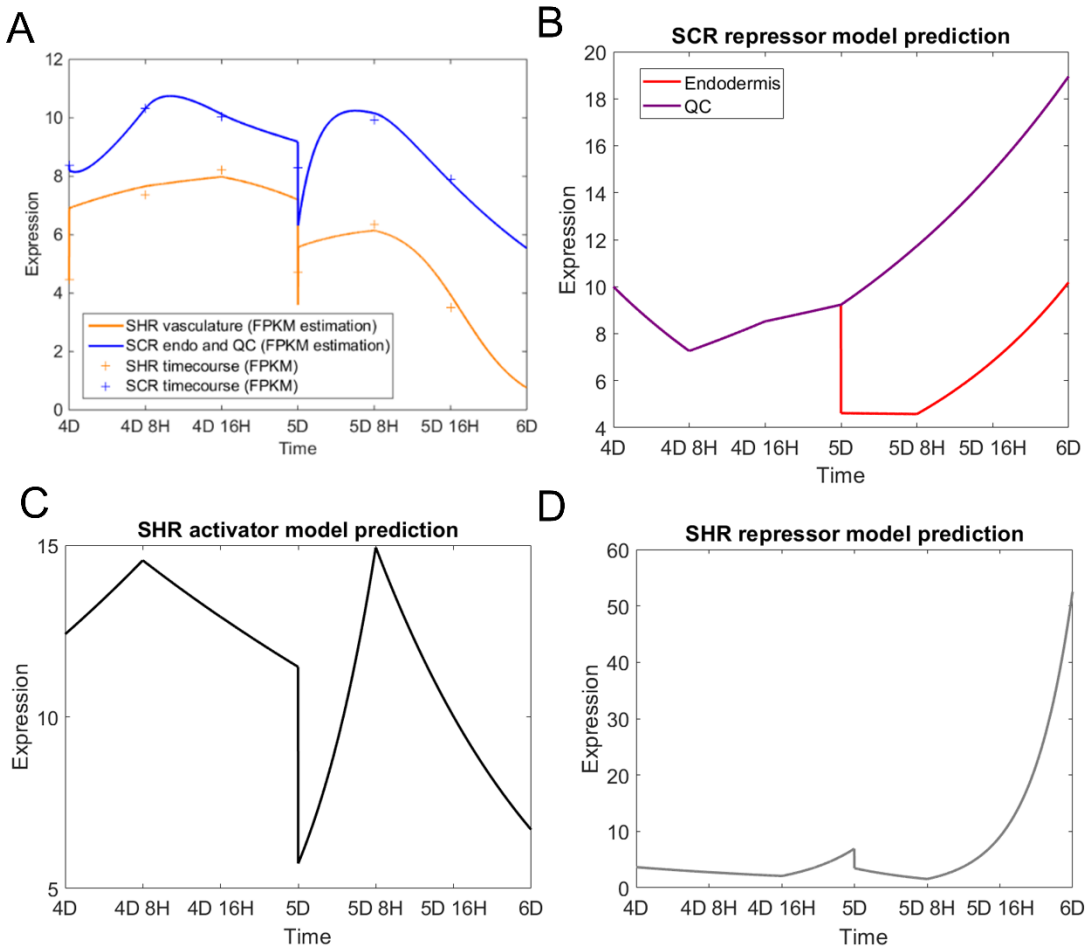

bioRxiv preprint doi: https://doi.org/10.1101/439331; this version posted October 9, 2018. The copyright holder for this preprint (which was not certified by peer review) is the author/funder. All rights reserved. No reuse allowed without permission.

Supplementary Figure 3: Model prediction of SHR, SCR, and their upstream SHR and their upstream regulators. (A) Model prediction of SHR in the vasculature (orange, solid line) and SCR in the endodermis and QC (blue, solid line). Crosses represent experimental data used to fit model. (B) Model prediction of the SCR repressor in the endodermis (red) and QC (purple). (C,D) Model prediction of the SHR repressor (C) and activator (D) in the vasculature.

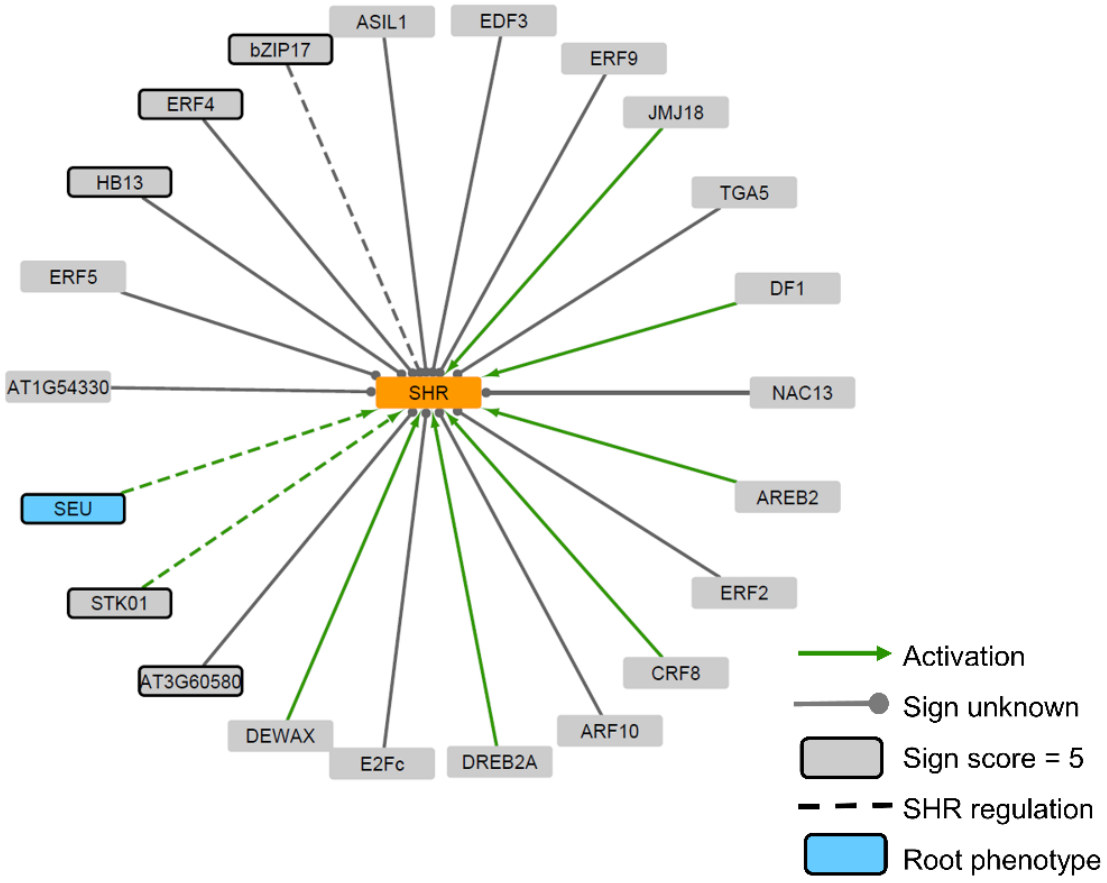

Supplementary Figure 4: Putative activators of SHR. Black solid boxes indicate the 6 genes with the maximum possible sign score of 5 (black borders). Dashed lines indicate three out of the 6 genes showing low SHR levels in their mutant lines. Blue box indicates one of the 3 genes, SEU, whose mutant shows root stem cell disorganization.

bioRxiv preprint doi: https://doi.org/10.1101/439331; this version posted October 9, 2018. The copyright holder for this preprint (which was not certified by peer review) is the author/funder. All rights reserved. No reuse allowed without permission.

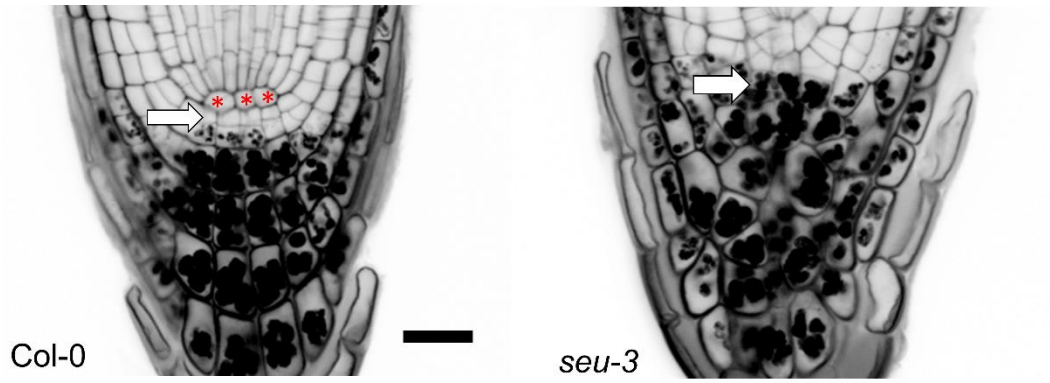

Supplementary Figure 5: mPSPI staining of *seu-3* mutants. Red * denote QC cells. White arrow denotes first layer of columella cells. Scale bar = 20 µm.

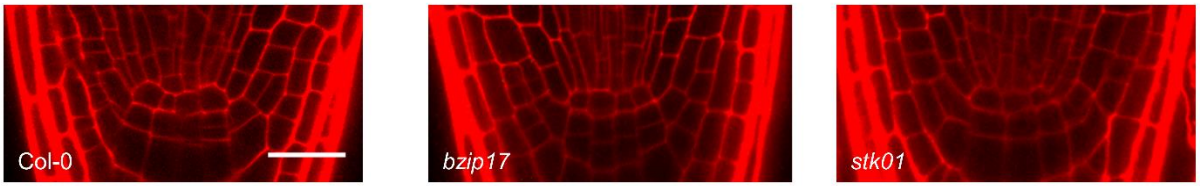

Supplementary Figure 6: Confocal images of additional SHR regulator mutants of interest. Cell walls are stained with propidium iodide (PI). Scale bar = 20 µm.

bioRxiv preprint doi: https://doi.org/10.1101/439331; this version posted October 9, 2018. The copyright holder for this preprint (which was not certified by peer review) is the author/funder. All rights reserved. No reuse allowed without permission.

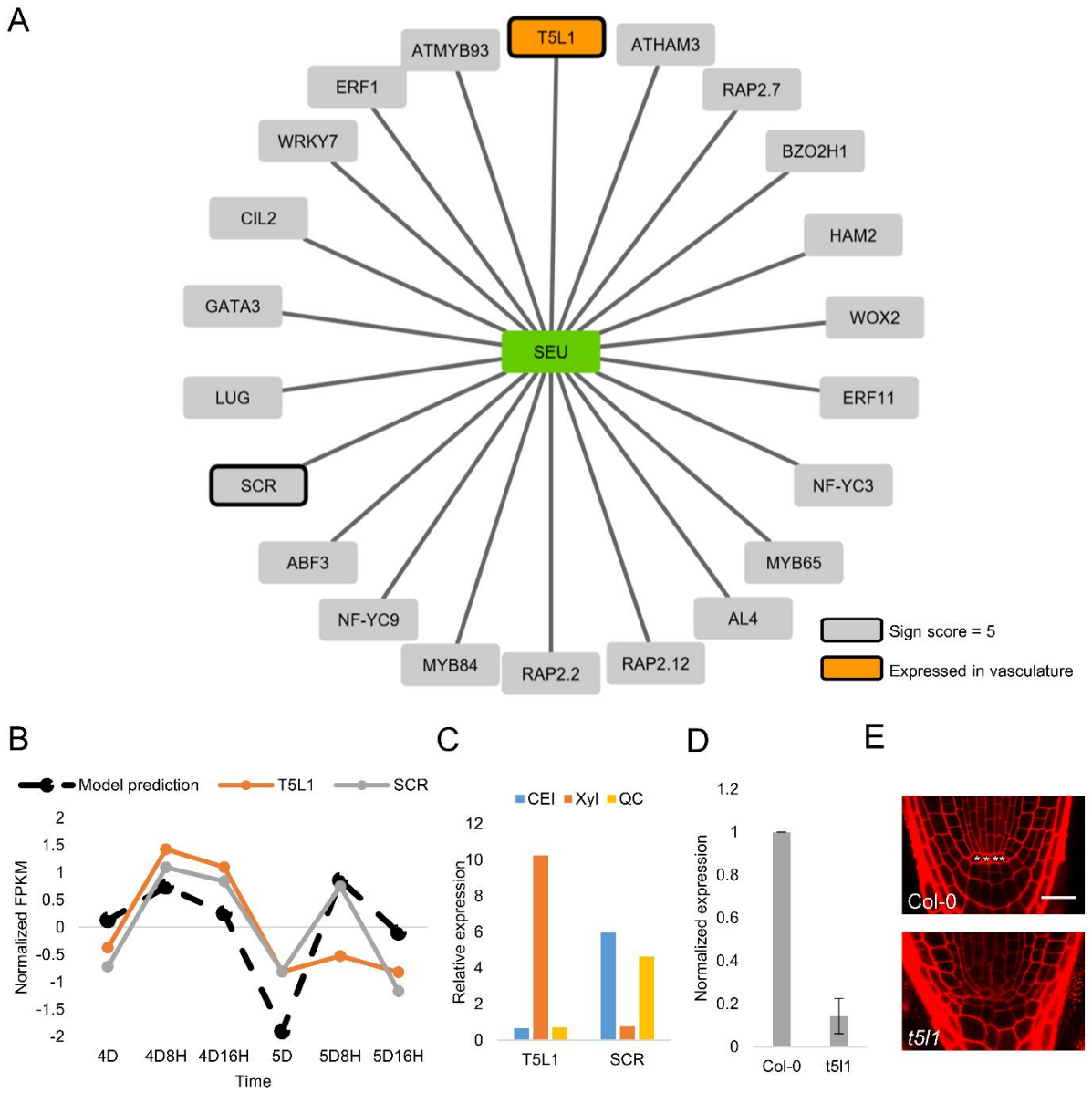

Supplementary Figure 7: T5L1 is a vasculature-specific, putative binding partner of SEU
(A) Representation of the 22 proteins identified as binding partners of SEU in Y2H analysis. Black solid boxes indicate two genes with the highest possible sign score of 5. Orange solid box highlights T5L1, which showed specific expression in the vasculature. (B) Black, dashed line indicates the normalized FPKM value of a SHR interactor as predicted by the model using the time course dataset. Two colored lines represent the normalized FPKM value of the two genes that have the maximum possible sign score of 5 based on the time course. (C) Bar graph showing the expression of the two best SEU binding partner candidates in Cortex-Endodermis Initials (CEI, blue), Xylem Initials (Xyl, orange), and Quiescent Center (QC, yellow). (D) SHR expression in the *t5l1* mutant measured using qPCR. Results are from two biological replicates. (E) Confocal images showing the wild-type root stem cell niche (top), *t5l1* mutant root with

bioRxiv preprint doi: https://doi.org/10.1101/439331; this version posted October 9, 2018. The copyright holder for this preprint (which was not certified by peer review) is the author/funder. All rights reserved. No reuse allowed without permission.

disorganized stem cell niche (bottom). * denotes QC cells in the wild type (Col-0) root. Scale bar = 20 µm.

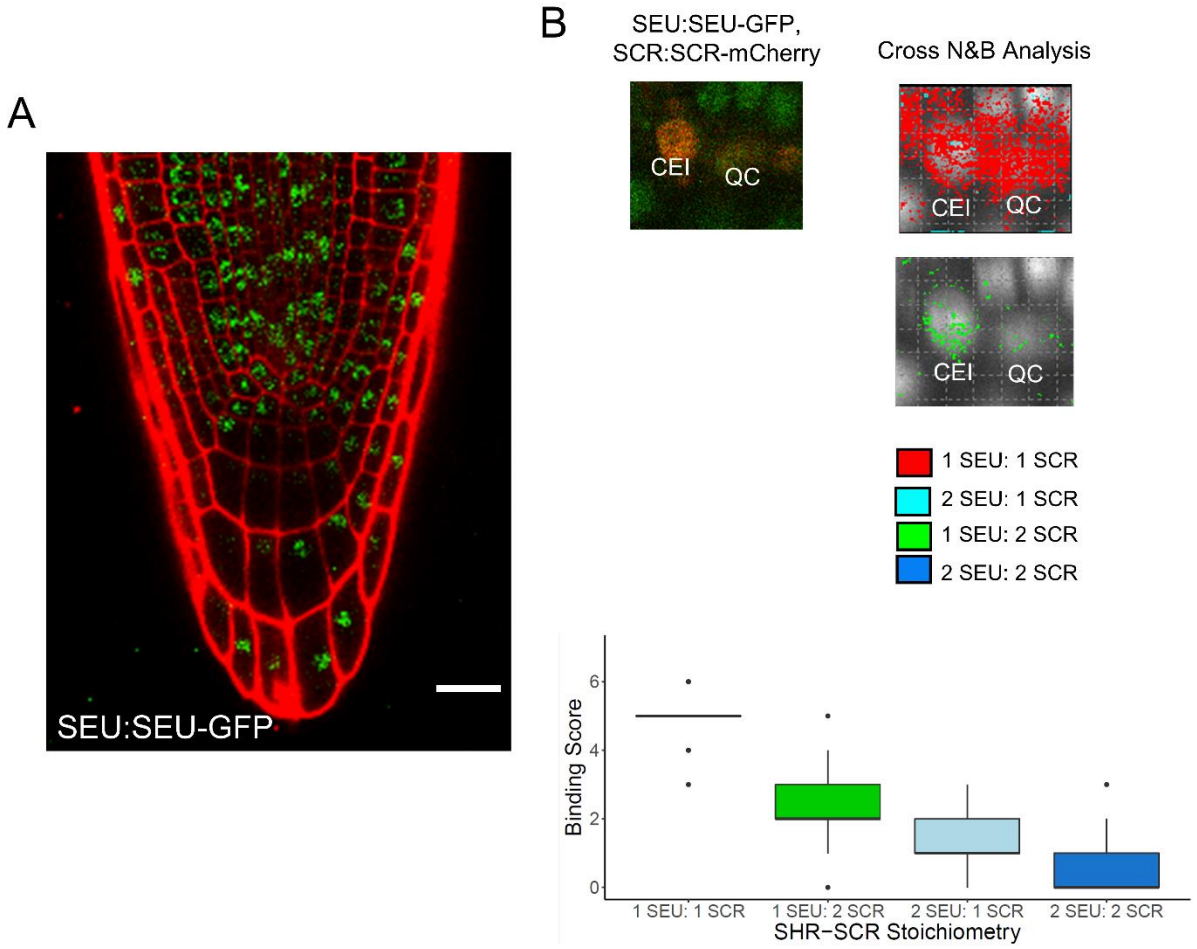

Supplementary Figure 8: SEU binds SCR in the QC and CEI. (A) Representative image of SEU:SEU-GFP expression in the root. Scale bar = 20 µm. (B) (top left) Representative image of SEU:SEU-GFP, SCR:SCR-mCherry in the CEI (left) and QC (right). (top right) Cross N&B analysis of image on the left. Red represents 1 SEU: 1 SCR, light blue represents 2 SEU: 1 SCR, green represents 1 SEU: 2 SCR, and dark blue represents 2 SEU: 2 SCR complex. (bottom) Quantification of complex binding scores (n=19).

bioRxiv preprint doi: https://doi.org/10.1101/439331; this version posted October 9, 2018. The copyright holder for this preprint (which was not certified by peer review) is the author/funder. All rights reserved. No reuse allowed without permission.

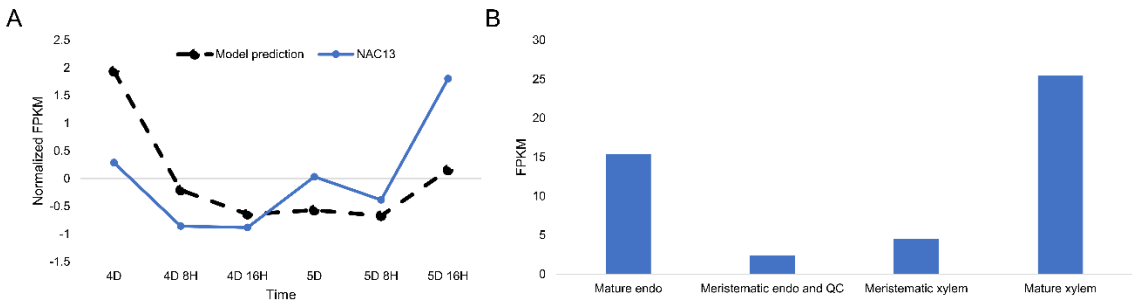

Supplementary Figure 9: Expression of NAC13 in the meristem. (A) Comparison of model prediction for repressor (black, dashed line) and NAC13 normalized FPKM from the timecourse dataset (blue, solid line). (B) Average FPKM of NAC13 in different regions of the root meristem.

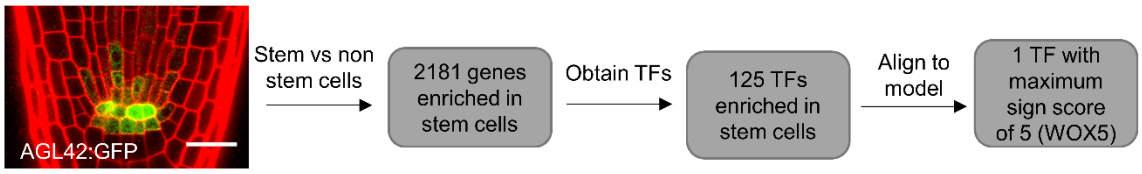

Supplementary Figure 10: Workflow of obtaining a transcriptomic profile of the root stem cells. GFP positive (stem cells) and negative (non-stem cells) cells were collected from roots expressing AGL42:GFP. Cuffdiff identified 2181 genes (125 TFs) enriched in the stem cells. The expression of the 125 TFs were aligned to the model prediction of the SHR repressor and identified 1 TF with the highest sign score, WOX5.

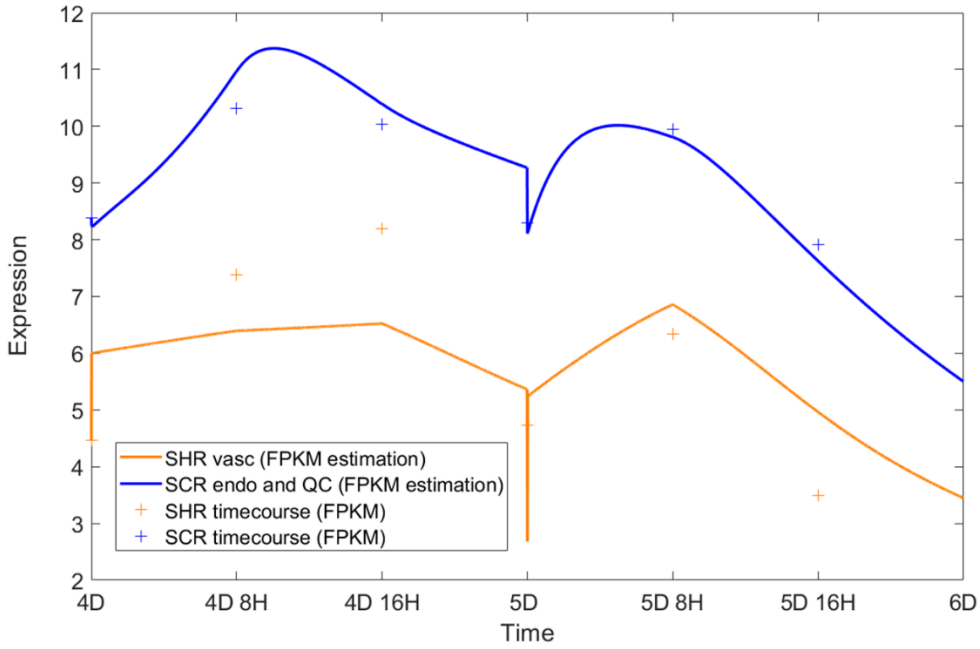

bioRxiv preprint doi: https://doi.org/10.1101/439331; this version posted October 9, 2018. The copyright holder for this preprint (which was not certified by peer review) is the author/funder. All rights reserved. No reuse allowed without permission.

Supplementary Figure 11: Final model simulation incorporating parameters estimated from SEU and WOX5 time course data. Solid lines represent model simulation, and daggers represent experimental data.

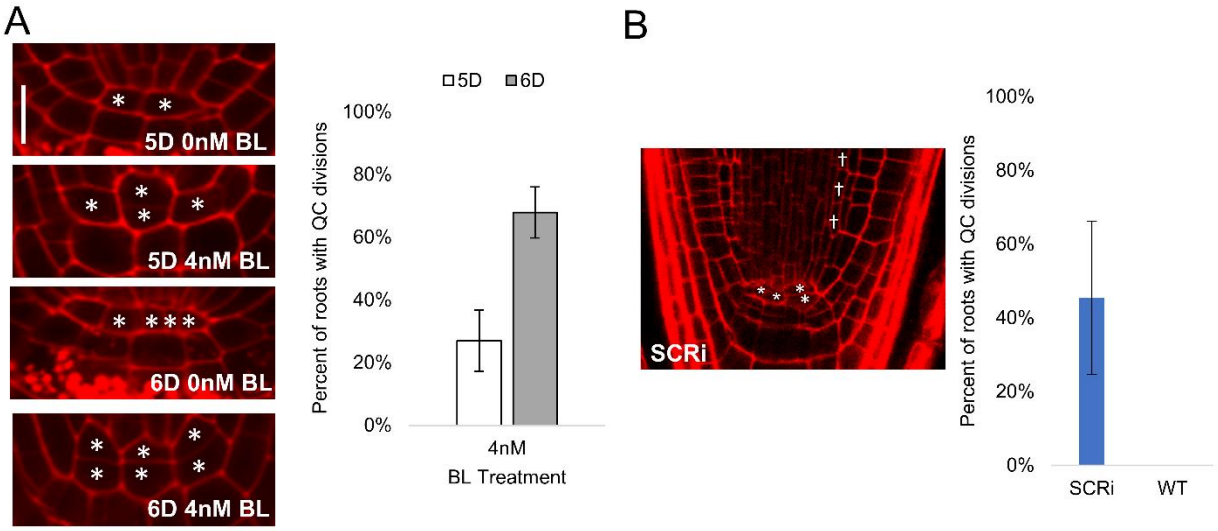

Supplementary Figure 12: Quantification of QC divisions in BL-treated and SCRi roots. (A) (left) Representative images of 5D (top half) and 6D (bottom half) plants with or without 4nM BL. * denotes QC cells. Scale bar = 10 µm. (right) Quantification of QC divisions in 4 nm BL treated roots at 5D (white bar) and 6D (gray bar). * denotes $p < 0.05$, Wilcoxon test. (B) (left) Representative image of a SCRi root at 5D with extra ground tissue layers (daggers). * denotes QC cells. (right) Quantification of the percent of SCRi and WT roots showing QC divisions at 5D.

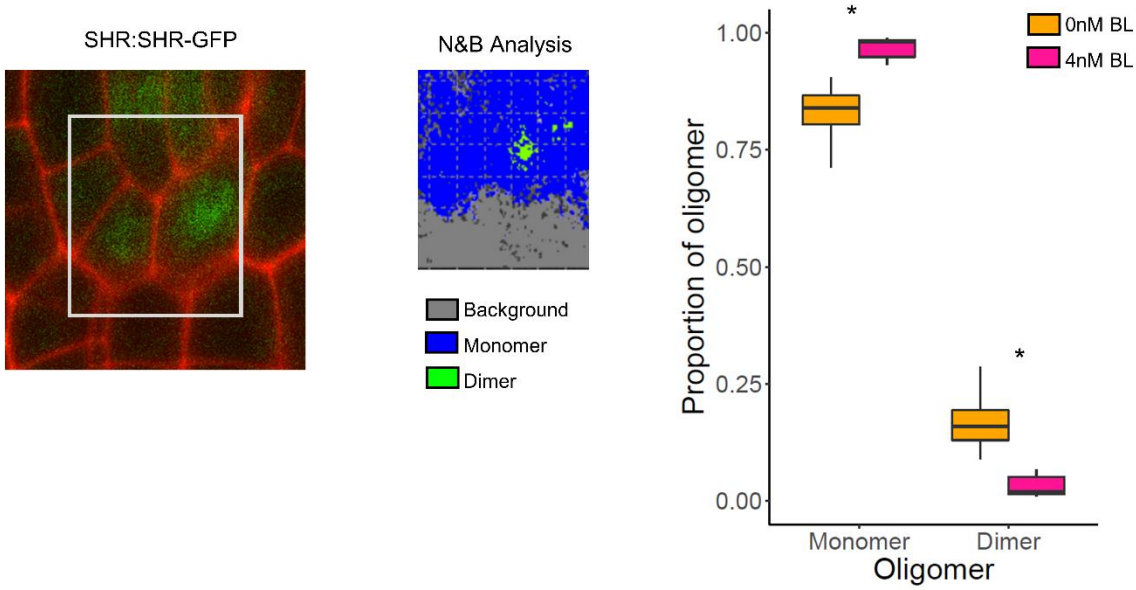

bioRxiv preprint doi: https://doi.org/10.1101/439331; this version posted October 9, 2018. The copyright holder for this preprint (which was not certified by peer review) is the author/funder. All rights reserved. No reuse allowed without permission.

Supplementary Figure 13: Quantification of SHR homodimer in BL-treated plants. (A) (left) Representative image of SHR:SHR-GFP in 5 day old plants treated with 4nM BL. Gray box represents ROI used for analysis. (middle) N&B analysis of ROI of image on the left. Grey represents background fluorescence, blue monomer, and green dimer. (right) Quantification of oligomeric state of SHR in plants treated with 0nM (left, n=15) or 4nM (right, n=6) BL. * denotes $p < 0.05$, Wilcoxon test

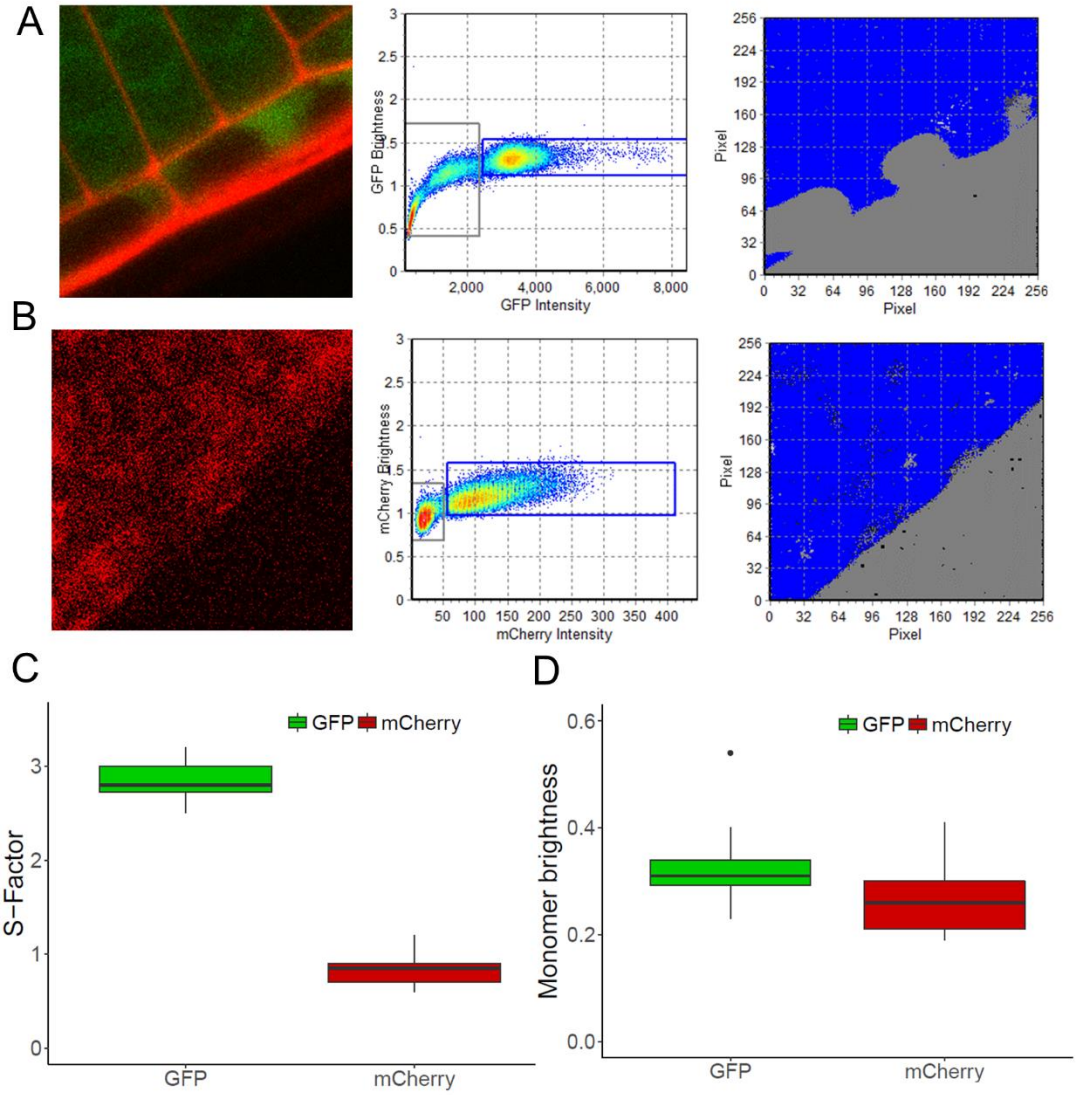

Supplementary Figure 14: Calibration for N&B using free GFP and mCherry lines. (A,B) Representative image (left), brightness plot (middle), and false-colored image (right) for 35S:GFP (A) and UBQ10:mCherry (B) lines. Blue represents monomer, grey represents background. (C) S-factor calculated for 35S:GFP (green) and UBQ10:mCherry (red). (D) Monomer brightness calculated for GFP (green) and mCherry (red).

bioRxiv preprint doi: https://doi.org/10.1101/439331; this version posted October 9, 2018. The copyright holder for this preprint (which was not certified by peer review) is the author/funder. All rights reserved. No reuse allowed without permission.

Supplementary Information

Model of SHR-SCR complex formation in the endodermis and QC
In the equations, $i = e$ for endodermis and $i = q$ for QC.

$$\frac{dS_v}{dt} = k_1 \frac{K_{XD}K_{YD} + K_{YD}X + XY}{K_{XD}K_{YD} + K_{YD}X + K_{XD}Y + XY} - a_i S_v - d_1 S_v$$

$$\frac{dS_i}{dt} = a_i S_v - d_{2i} S_i$$

$$\frac{dS_{2i}}{dt} = k_{2i}(C_i) S_i^2 - d_3 S_{2i}$$

$$\frac{dC_i}{dt} = k_{3i}\left(\frac{K_{1Di}^2 K_{2Di} C_i + K_{1Di}^2 C_{2i} + K_{1Di}K_{2Di}(SC)_i + K_{2Di}(S_2C)_i + K_{1Di}(SC_2)_i + (S_2C_2)_i}{K_{1Di}^2 K_{2Di}^2 + K_{1Di}K_{2Di}^2 S_i + K_{2Di}^2 S_{2i} + K_{1Di}^2 K_{2Di} C_i + K_{1Di}^2 C_{2i} + K_{1Di}K_{2Di}(SC)_i + K_{2Di}(S_2C)_i + K_{1Di}(SC_2)_i + (S_2C_2)_i}\right)$$
$$+ k_{3i}\left(\frac{K_{ZDi}}{K_{ZDi} - Z_i}\right) - d_{4i} C_i$$

$$\frac{dC_{2i}}{dt} = k_{4i} C_i^2 - d_{5i} C_{2i}$$

$$\frac{d(SC)_i}{dt} = k_{5i} S_i C_i - d_{6i}(SC)_i$$

$$\frac{d(S_2C)_i}{dt} = k_{6i} S_{2i} C_i - d_{7i}(S_2C)_i$$

$$\frac{d(SC_2)_i}{dt} = k_{7i} S_i C_{2i} - d_{8i}(SC_2)_i$$

$$\frac{d(S_2C_2)_i}{dt} = k_{8i} S_{2i} C_{2i} - d_{9i}(S_2C_2)_i$$

$$\frac{dX}{dt} = k_9 X$$

$$\frac{dY}{dt} = k_{10} Y$$

$$\frac{dZ_i}{dt} = k_{11} Z_i$$

where $a_i = \frac{D_i}{A_v}$ and $k_{2i}(C_i) = \frac{L_i}{1 + e^{-s(C_i - C_0)}}$.

bioRxiv preprint doi: https://doi.org/10.1101/439331; this version posted October 9, 2018. The copyright holder for this preprint (which was not certified by peer review) is the author/funder. All rights reserved. No reuse allowed without permission.

Supplementary Tables

Supplementary Table 1: Sensitivity analysis of SHR-SCR model

Supplementary Table 2: Parameter values used in SHR-SCR model

Supplementary Table 3: FPKM values from the time course of the root meristem

Supplementary Table 4: Candidate SHR regulators and their sign scores

Supplementary Table 5: Differentially expressed genes in the *seu-3* mutant

Supplementary Table 6: Yeast Two Hybrid results

Supplementary Table 7: Sign score of candidate SEU interactors

Supplementary Table 8: Sign scores of the 125 TFs differentially expressed in the stem cells

Supplementary Table 9: Differentially expressed genes in the *wox5-1* mutant

Supplementary Table 10: SHR-SCR model parameters estimated using SEU and WOX5 time course data.

Supplementary Table 11: Expression of SCR in the QC and endodermis

Supplementary Table 12: Parameter sets generated from time course estimation.

Supplementary Table 13: Primers used in this study.